Night-time gravity waves detected with multi-frequency airglow imager

A thesis submitted in fulfilment of the
requirements for the degree of

MASTER OF SCIENCE

of

RHODES UNIVERSITY

Department of Physics and Electronics at Rhodes University

by

Karabo Pebane Machubeng

December 2020

Abstract

This thesis shows the statistics of atmospheric gravity waves (AGWs) observed in the OI emission 557.7 nm at ∼97 km altitude using an all-sky imager based in Sutherland, South Africa (32.37° S, 20.81° E) in the year 2017. The wavelengths were determined using the propagation vector method, velocity was determined using the cross correlation of 1D FFT and the period was determined using the equation that relates wavelength and velocity. It was found that the horizontal wavelength in summer was almost evenly distributed between 10 and 40 km and for autumn, winter and spring were mostly between 10 and 30 km. The favoured speeds were between 40 and 50 m/s in autumn, as well as 30 and 50 m/s in summer, but the AGWs in winter had a bimodal speed distribution of 20 - 40 and 50 - 70 m/s. The majority of periods observed in all seasons were less than 20 minutes with a dominant peak of 5 - 10 minutes in autumn and spring. There was no favoured propagation direction for spring, but AGWs favoured a southeastward propagation in summer, and a southward propagation in autumn and winter.

Dedication

I dedicate this thesis to my parents Naniki and Enos Machubeng. Thank you for allowing me to follow my dreams.

Acknowledgements

I would like to first thank God for his grace during this period in my life. I would like to extend my heartfelt gratitude to my supervisors, Dr Zama Katamzi-Joseph and Professor Michael Kosch. This project would not have been accomplished without their tireless guidance and leadership during the course of my studies. I wish to thank the management of South African National Space Agency (SANSA) for granting me the opportunity to further my studies through their financial assistance. This project would not be possible without the data from the Boston University and as such I would like to thank them for allowing us the opportunity to use their data to produce the results discussed in this thesis. I would also like to thank Dr Pierre Cilliers, Mr Michael Heyns, Mr Dakalo Mashao, Miss Tsige Atilaw, Mr Moment Mahlangu and Mr Thabelo Sivhe for their contributions and support during this period of study. Finally, I would like to thank my family for their continuous support and prayers during this period.

Contents

List of Figures

List of Tables

Chapter 1

Introduction

The earth's atmosphere is made up of a mixture of gases such as molecular nitrogen at 78% volume and molecular oxygen at a 21% volume. Other constituents such as water vapor, carbon dioxide, and ozone as well as other minor constituents make up the remaining 1% of the atmosphere. Solar radiation is the most important source of energy on earth and in the earth's atmosphere. As much as it is the source of life in the biosphere it also acts as the main driving force for the dynamics of the atmosphere. The two constituents of the atmosphere that mainly absorb solar radiation are oxygen and nitrogen. They are dissociated and ionized by the shorter wavelength radiation with the minor atmospheric constituents such as water vapour and carbon dioxide also contributing to the absorption of solar radiation as well as the active chemistry of the atmosphere [McEwan & Phillips, 1975; Leckner, 1978; Solomon et al., 1998; Brasseur & Solomon, 2006].

The earth's atmosphere has layers that are subdivided based on either its chemical composition, temperature profile which can be identified empirically, or physical processes that occur in that region. The names of the layers are denoted with "sphere" to indicate the region and "pause" to indicate the upper boundaries of each layer. Figure 1 presents a typical temperature profile showing how the temperature varies with altitude and layers associated with this trend. The troposphere reaches up to 10 km, stratosphere is found at approximately 11 km up to 50 km, mesosphere at a height above the stratopause up to approximately 85 km, and above the mesopause starts the thermosphere. Temperature variation with altitude is one way to classify the layers but other properties are ozone density, solar ionization, and gas mixture, for layers such as the ionosphere and the magnetosphere [Chapman, 1950; Brasseur & Solomon, 2006].

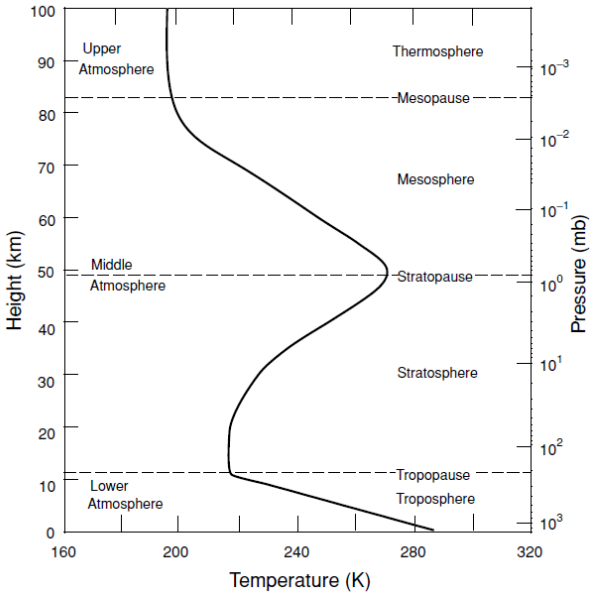

Figure 1.1: Layers of the atmosphere as defined using a temperature profile [Tricoli, 2015]

As shown in figure 1.1, the temperature in the troposphere decreases with increasing altitude up to a minimum called the tropopause, the location of which varies with season and latitude. It's location at the equator is at about 16 km with a first temperature minimum of ∼190 K, while in the polar regions its altitude can be found at about 8 km with a mean temperature of approximately 220 K [Brasseur & Solomon, 2006]. The temperature decrease in the troposphere has a constant lapse rate, i.e. the rate of decrease of temperature with altitude, and its global mean is roughly 6.5K/km [Salby, 1996]. The troposphere has uniform composition and a pressure that decreases as the altitude increases. It contains weather processes driven by surface heating. The emission and absorption capabilities of infrared radiation by water vapor, carbon dioxide, and ozone molecules make energy transfer between the atmospheric layers efficient [Brasseur & Solomon, 2006; Salby, 1996].

The temperature in the stratosphere increases with altitude (see figure 1.1) and results in a positive lapse rate. The increase in temperature reflects the ozone heating that results from the absorption of solar UV. The temperature in the stratosphere is found to be about 220 K in mid-latitudes (i.e. geomagnetic latitude between 30°and 60°) [Brasseur & Solomon, 2006; Moon et al., 2017]. The ozone which is found in the middle atmosphere (i.e. stratosphere and mesosphere) is the only atmospheric species that effectively absorbs ultraviolet solar radiation

from about 250 – 300 nm, protecting animal and plant life from exposure to the harmful radiation [Brasseur & Solomon, 2006]. Other differences of the stratosphere from the troposphere are that only weak vertical motions are involved due to the increased temperature and radiative processes, which dominate in this layer. The upper boundary of the stratosphere is the stratopause which is found at an altitude of about 50 km where a temperature maximum of about 270 K is reached [Brasseur & Solomon, 2006; Salby, 1996].

The mesosphere is the layer found just above the stratopause where the temperature decreases with altitude, as can be seen in figure 1.1, and ozone heating becomes less. In this layer the temperature ranges from a high of 263 K in the stratopause to a low of 185 K at the mesopause, making it the coldest layer of the atmosphere [Roble, 1995]. Atmosphere meteor trails can form in this layer as well as in the lower layers of the ionosphere during the daytime. The mesopause is the upper boundary of the mesosphere and is found at about 85 km altitude where a second temperature minimum can be found [Brasseur & Solomon, 2006; Salby, 1996].

The thermosphere is the layer above the mesopause found at approximately 100 km. The lower part of the thermosphere has a temperature that increases upward with a gradient of about 9 K/km [Salby, 1996; Brasseur & Solomon, 2006; Chamberlain, 2016]. The temperature increases steadily in this layer and there is a downward flow of heat in the region with a positive temperature gradient [Salby, 1996; Chamberlain, 2016]. The ionosphere is a partially ionized gas that surrounds the earth at an altitude range of about 50 - 1000 km and acts as an interface between the atmosphere and space [Kelley, 2009].

The atmosphere is a firmly fixed and stratified fluid that has the ability to support and propagate wave motions, such as atmospheric gravity waves, tides and planetary waves. Atmospheric gravity waves (AGWs) are types of waves that occur in the atmosphere whose restoring force is gravity. They affect the behaviour of the atmosphere and represent important dynamic processes that facilitate vertical and horizontal energy transfer between different layers of the atmosphere [Andrews et al., 1987; Nappo, 2013]. In the ionosphere, atmospheric gravity waves manifest as traveling ionospheric disturbances (TIDs), which appear as a decrease and increase of the ionospheric electron content or electron density as the ionospheric plasma moves up and down. In other words, TIDs are quasi-periodic perturbations observed at ionospheric altitudes but caused by the passage of gravity waves in the lower atmospheric regions. In addition to

gravity, the restoring force for TIDs also includes the magnetic field because charge particles are normally constrained to move parallel to the magnetic field only. This is especially true at higher altitudes in the F-region ionosphere where the ion-neutral collision frequency is low. [Davies, 1990; Shiokawa et al., 2003; Ssessanga et al., 2015].

AGWs have been observed in different parameters of the atmosphere, such as temperature and airglow intensity. Airglow is the light emitted by the upper atmosphere, other than that known as the polar aurora, through chemical processes [Chapman, 1950; Elvey, 1950]. The phenomenon is believed to have first been discovered prior to the 1800s. Its existence was established using photometry by Yntema [1909] who named it Earthlight. Chapman [1950] was one of the first scientists to theoretically explain the airglow and the features that are related to the phenomenon [Chattopadhyay & Midya, 2006]. Airglow can be seen near 85 - 90 km for the hydroxyl (OH) bands (<200 nm), near 90 km for sodium (589.3 nm) and near 95 - 100 km for the atomic oxygen green line (557.7 nm) and near 160 - 350 km for the atomic oxygen red line (630.0 nm) [Hecht, 2004; Chattopadhyay & Midya, 2006; Kamide & Chian, 2007; Martinis et al., 2018]. The emissions are a result of atomic oxygen reacting with itself and/or other species present in those altitudes [Hecht, 2004]. Dissociative recombination of the particles produced by ultraviolet absorption of sunlight is the most common mechanism. The typical atmospheric emission processes for sodium, hydroxyl, and oxygen green and red line airglow are [Chapman, 1950; Takahashi et al., 1992; F. J. Garcia, 1999; Makela & Kelley, 2003; Brasseur & Solomon, 2006; Martinis et al., 2018]:

(a) Sodium

$$O + O_2(+M) \longrightarrow O_3(+M) \tag{1.1}$$

$$Na + O_3 \longrightarrow NaO + O_2 \tag{1.2}$$

$$NaO + O \longrightarrow Na^*(^2P) + O_2 \tag{1.3}$$

$$Na^*(^2P) \longrightarrow Na(^2S) + 589.0 \text{ nm photon} \tag{1.4}$$

(b) Hydroxyl (OH)

$$H + O_3 \longrightarrow OH^*(v \leq 9) + O_2 \tag{1.5}$$

$$OH^* \longrightarrow OH + 845.0 \text{ nm photon} \tag{1.6}$$

(c) Oxygen green line $O(^1S)$ excited to their ^1S state through three body collisions such as:

$$O + O + M \longrightarrow O_2^* + M \tag{1.7}$$

this reaction can be followed by photo-radiative decay

$$O_2^* \longrightarrow O_2 + 557.7 \text{ nm photon} \tag{1.8}$$

where "M" denotes a third body which could be either N_2 molecule or O atom

(d) Oxygen red line $O(^1D)$ excited to their (^1D) state through:

$$O_2 + e^- \longrightarrow O + O^* \tag{1.9}$$

followed by photo-radiative decay

$$O^* \longrightarrow O + 630.0 \text{ nm photon} \tag{1.10}$$

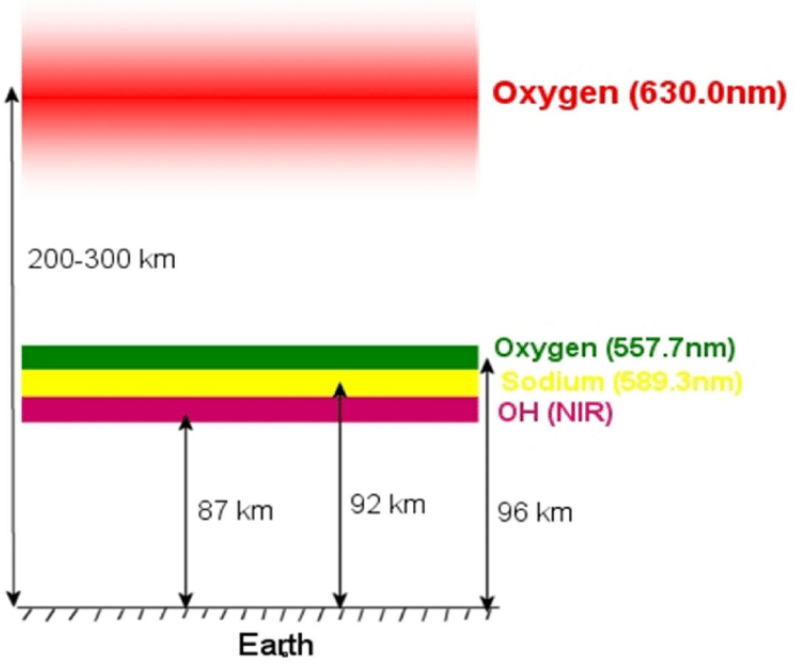

Figure 1.2: An illustration showing the heights of the various airglow layers seen from a CCD imager and the wavelengths of the emissions (not to scale) [Chapagain, 2011].

Many climatological and case studies of AGWs and TIDs have been done using various instruments, such as ionosondes [Klausner et al., 2009; Amorim et al., 2011; Krankowski et al.,

2011], global navigation satellites systems (GNSS) [Mukhtarov et al., 2013; Habarulema et al., 2016; Arikan & Yarici, 2017], and airglow imagers [Shiokawa et al., 2003; Otsuka et al., 2004; Makela et al., 2010], in order to understand the nature of these waves/disturbances. However, until Martinis et al. [2019] only a few case studies of large scale TIDS have been conducted over the African/South African region using GNSS observations [Habarulema et al., 2013; Katamzi & Habarulema, 2014]. Martinis et al. [2019] was the first study to report medium scale TIDs using ground based 630.0 nm airglow measurements over South Africa, which was compared to conjugate measurements over Italy. As a result, more studies of these waves, in particular climatological studies using different instruments (such as optical instruments in the form of airglow imagers), will help us better understand how these waves alter the neutral atmosphere-ionosphere dynamics, which makes it challenging to accurately predict or model the atmosphere-ionosphere, and how they affect aerospace and ground-based radio systems. In addition, it is important to know the properties of these waves in order to understand their theoretical framework.

Boston University has installed all-sky imagers at different observatories considered to be at opposite ends of the geomagnetic field lines of each hemisphere (i.e. conjugate points), including an observatory in South Africa and its conjugate in Italy. The multi-wavelength all-sky imager used in this project was installed at the South African Astronomical Observatory (SAAO) in Sutherland, South Africa (32.37°S, 20.81°E, magnetic latitude 40.7°S) in July 2016. As the first of such instruments in South Africa, it offers an opportunity to study the morphology and distribution of AGWs, TIDs and other atmospheric disturbances/waves at different layers of the atmosphere in detail not previously possible with instruments such as the ionosondes and GNSS receivers [Martinis et al., 2018, 2019].

1.1 Aim of project

The aim of the project is to determine the properties of night-time atmospheric gravity waves (AGWs) over South Africa using a multi-wavelength measurement of the airglow from the all-sky imager (ASI) in Sutherland. The objectives are:

• determine the waves' parameters, such as period, wavelength, speed and propagation azimuth, from measurements of the 557.7 nm airglow emissions,

• determine statistical characteristics of these parameters, and

• discuss some mechanisms through which the waves are generated, especially during quiet geomagnetic conditions.

1.1.1 Structure of the Thesis

The chapters of this project are arranged as follows:

• Chapter 2 gives the theoretical background and morphology of the mesosphere and atmospheric gravity waves studied.

• Chapter 3 discusses the instrument and the methodology used to analyse the data used. This discusses the image processing procedures as well as the spectral analysis used to calculate the gravity wave characteristics.

• Chapter 4 analyses the results obtained from the methods discussed in Chapter 3 and discusses the seasonal characteristics of the gravity waves.

• Chapter 5 summarises the conclusions and gives future works of this study

Chapter 2

Mesosphere and Atmospheric Gravity Waves

This chapter explores further the background theory of the mesosphere and the atmospheric gravity waves (AGWs), showing the derivation of the dispersion relation for AGWs to demonstrate the difference between them and acoustic waves in the atmosphere.

2.1 Mesosphere

The various layers in the atmosphere were discussed in Chapter 1 highlighting their different characteristics. The layer we are most focused on in this project is the mesosphere because the AGWs studied in this project propagate in this layer. It is the least understood of the layers because of its complex dynamics, and the lack of experimental observations related to the layer. For recap purposes, the mesosphere is found above the stratosphere located at an altitude range between 50 km and 80 km, where the temperature decreases as the altitude increases. The mesosphere is the product of the turbulent mixing of conditionally stable air and the positive lapse rate of ozone concentration which is characteristic of this layer [Webb, 1966].

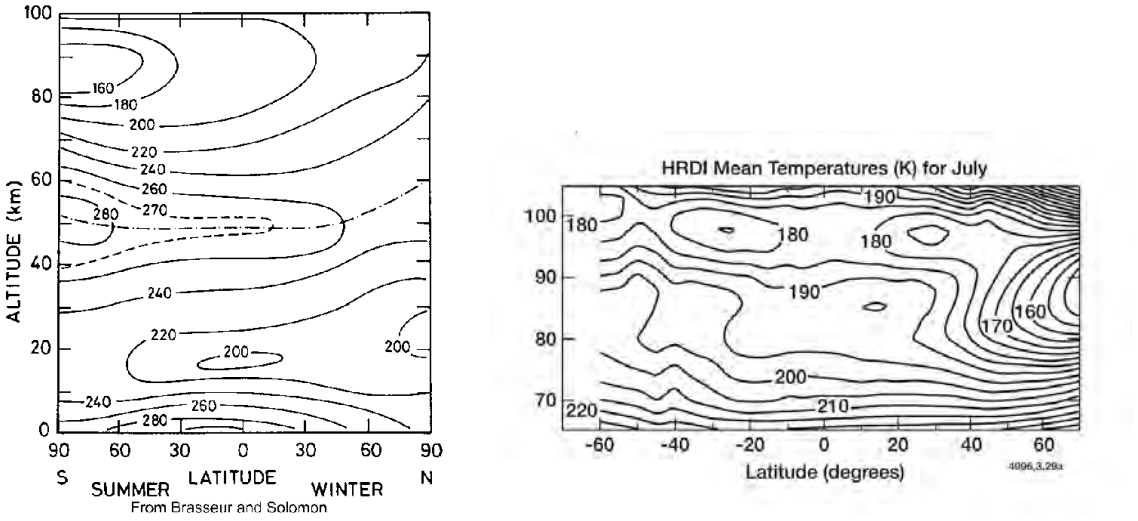

Figure 2.1: The averaged temperature in the mesosphere [Brasseur & Solomon, 2006].

The mesopause is the region separating the mesosphere below it from the thermosphere above it. It is defined by the temperature minimum which varies seasonally and with latitude as seen in Figure 2.1 (as obtained from Brasseur & Solomon [2006]) where the image on the left shows the observed temperature for December and the image on the right shows the temperature in July. In the regions surrounding the equator at all seasons and midlatitudes, the transition takes place at an altitude of ∼100 km [Brasseur & Solomon, 2006]. At the winter pole the temperature in the mesopause reaches 180 – 220 K at around 100 km. During summer at high latitudes the mesopause is located near 85 - 100 km and the temperature at the northern hemisphere pole can reach values as low as 120 - 140 K [Brasseur & Solomon, 2006]. The manner in which the mesopause is structured is attributed to the detailed relationship between the dynamics, radiative transfer, and photochemistry [A. K. Smith, 2004; Brasseur & Solomon, 2006].

Radiative processes contribute more to the energy in the area neighbouring the mesosphere, but other processes to look out for are adiabatic heating and cooling mechanisms related to the large scale transfer of heat horizontally through the atmosphere. Other processes such as chemical heating and energy loss to space by radiative emissions also play a key role in the energetics of the mesopause [D. C. Fritts, 1995; Brasseur & Solomon, 2006]. The mesopause is partial to the internal variability produced by atmospheric gravity waves that propagate upwards [Brasseur & Solomon, 2006].

2.2 Atmospheric Gravity Waves

Atmospheric gravity waves are propagating atmospheric waves whose restoring force is gravity. AGWs in the mesosphere and lower thermosphere have been studied since being perceived to be responsible for the structure of the mesosphere and lower thermosphere (MLT) [Hines, 1960]. The Earth's atmosphere is almost always stably stratified and can thus be considered to be a fluid. A fluid that is steadily stratified is one in which the density of the fluid increases with depth. A stably stratified fluid has a trait whereby it supports and propagates wave motion. It is safe to assume that the atmosphere always contains AGWs as it is believed to always be steadily stratified except for the thin layer near the earth's surface, i.e. the terrestrial boundary layer [Nappo, 2013].

The large scale circulation, thermal and constituent structure of the MLT is affected by the AGWs which also contribute to the variability of the region. The waves that occur in the MLT region propagate upwards and that's when Earth's gravity becomes a restoring force in the propagation of these waves. The period of these waves ranges between 5 minutes and 3 hours, and horizontal wavelengths range from 50 to 500 km with vertical wavelengths having a range from 5 to 10 km in the mesosphere [Mondal et al., 2019].

Energy and momentum are transferred through the different layers of the atmosphere by atmospheric gravity waves. Through breaking and/or saturation of the waves, they can transport momentum and energy to upper atmosphere [Hines, 1960; Bretherton, 1969; D. C. Fritts & Alexander, 2003; Costantino et al., 2015; Mondal et al., 2019]. Small-scale gravity waves are waves with wavelengths less than 100 km and short periods typically less than 30 min. In the MLT region small-scale waves are caused by the breaking of gravity waves as a result of neutral instability associated with internal gravity waves [Winters & Riley, 1992; Nakamura et al., 1999]. Their interaction with large scale planetary waves amplifies them and they go on to disturb the ionosphere dynamics. The classification of gravity waves is important in studying the upper atmosphere and the dynamics that occur in the region in which they are observed [Vincent, 2015].

Waves have a wide variety of forms seen stirring in different directions. Figure 2.2 shows a representation of what the waves would look like as described by Hines & Hines [1974]. The waves could be moving horizontally or propagating upwards or downwards throughout the field

of view. Some of the waves could be seen spread out throughout the field of view as they propagate from one point to the next.

Figure 2.2: A surrealistic representation of atmospheric gravity waves [Hines & Hines, 1974].

2.3 Brunt-Väisälä frequency

In the Earth's atmosphere the oscillations from AGWs play a major role in several dynamic processes. These waves are responsible for the coupling that occurs both vertically and horizontally in the atmosphere resulting in the atmosphere being a single entity [Roble, 1995; Taylor et al., 1997]. An important prerequisite of the atmosphere is static stability which allows for vertical propagation of gravity waves. The measure of the static stability of the medium is the buoyancy oscillation in a stably stratified fluid, i.e. the Brunt-Väisälä frequency [Beer, 1978; Roble, 1995; Nappo, 2013]. In other words it is the frequency at which a vertically displaced parcel will oscillate within a statically stable environment [Dolas & Kishore Kumar, 2009].

2.3.1 Brunt-Väisälä frequency

To derive the Brunt-Väisälä frequency, let F be the force acting on the parcel of atmosphere which has volume V and initial position (z,p), where

$$F = \text{ma}. \tag{2.1}$$

Assume the air parcel moves from initial position to point B, where B = (z + z$'$, $p-\Delta$ p) and z' = dz/dt. The net force acting on the air parcel is the difference between the weight and buoyancy force [Nappo, 2013]:

$$F = F_b - F_g \tag{2.2}$$

where $F_b = mg$, $F_g = m^{'}g$, $m = \rho V$, $m' = \rho' V$, ρ being the density of the surrounding air, and ρ', is the density of the air parcel. Therefore equation 2.2 becomes

$$m' \frac{d^2 z'}{dt^2} = g(m - m') \tag{2.3}$$

$$\rho' V \frac{d^2 z'}{dt^2} = g(\rho V - \rho' V) \tag{2.4}$$

$$\rho' \frac{d^2 z'}{dt^2} = g(\rho - \rho') \tag{2.5}$$

$$\frac{d^2 z'}{dt^2} = g(\frac{\rho - \rho'}{\rho'}). \tag{2.6}$$

At level z_0, the air parcel has the same density as its environment,

$$\rho'(z_0) = \rho(z_0), \tag{2.7}$$

for small change in displacement, the density along z can be approximated by Taylor series expansion.

$$\rho'(z_0 + \Delta z) \approx \rho(z_0) + \frac{\partial \rho'}{\partial z}\Delta z = \rho(z_0) + \frac{\partial \rho'}{\partial P'}\frac{\partial P'}{\partial z}\Delta z \tag{2.8}$$

the last term of equation 2.8 utilises the hydrostatic law, where ρ is proportional to P. This implies that as the air parcel rises, its pressure adjusts promptly to the pressure of the surrounding environment, so that

$$P' = P \tag{2.9}$$

In hydrostatic equilibrium, density of an object is given by

$$\rho = \frac{P}{RT} \qquad \text{and} \qquad \rho' = \frac{P'}{RT}, \tag{2.10}$$

therefore substituting equation 2.10 into 2.6 and using equation 2.9, yields

$$\frac{d^2z'}{dt^2} = g\left(\frac{\frac{P}{RT} - \frac{P'}{RT'}}{\frac{P'}{RT'}}\right)$$

$$\frac{d^2z'}{dt^2} = g(\frac{\frac{1}{T} - \frac{1}{T'}}{\frac{1}{T'}})$$

$$\frac{d^2z'}{dt^2} = g(\frac{T' - T}{T}). \tag{2.11}$$

Let the ambient temperature be:

$$T = T_0 + \Gamma z' \tag{2.12}$$

where Γ is the adiabatic lapse rate, given by $\Gamma = -\frac{dT}{dz}$. If the initial temperature at z is T_0 then the temperature at $z + z'$ will be

$$T' = T_0 + \Gamma_d z' \tag{2.13}$$

where Γ_d is the dry adiabatic lapse rate. The difference between equation 2.12 and equation 2.13, gives

$$T' - T = (\Gamma_d - \Gamma)z'. \tag{2.14}$$

Substitute equation 2.14 into equation 2.11

$$\frac{d^2z'}{dt^2} = \frac{g}{T}(\Gamma_d - \Gamma)z'. \tag{2.15}$$

Using the equation of motion in Newtonian mechanics, equation 2.15 can be written as

$$\frac{d^2z'}{dt^2} + \omega_B^2 z' = 0$$

where ω_B^2 is the Brunt-Väisälä frequency and is denoted by the equation below.

$$\omega_B^2 = \frac{g}{T}(\frac{dT}{dz} - \Gamma_d). \tag{2.16}$$

Equation 2.16, gives us the nature the stability of the atmosphere; that's if ω_B^2 is positive, then atmosphere is stable, otherwise it's unstable for negative ω_B^2.

Temperature at the stratopause, which in the lower mesosphere is about 263 K at 45 $\pm$ 5 km, and at 90 km it is $\sim$ 185 K [Beer, 1978; Roble, 1995]. Also Γ_d in the mesosphere is -9.8 K/km

[Roble, 1995]. Therefore the Brunt-Väisälä frequency can be calculated from equation 2.18, where $T_0 = 263$ K, T = 185 K, $z_0 = 45$ km, z = 90 km and g = 9.8 ms^{-2}

Calculating the observed temperature gradient:

$$\begin{aligned}\frac{dT}{dz} &= \frac{T - T_0}{z - z_0} \\ &= \frac{185 - 263}{90 - 45} \\ &= -1.73 \text{ K/km}\end{aligned}$$

Calculating the Brunt-Väisälä frequency:

$$\begin{aligned}\omega_B^2 &= \frac{g}{T}(\frac{dT}{dz} - \Gamma_d) \\ &= \frac{9.8 \text{ ms}^{-2}}{185 \text{ K}}(-1.73 - (-9.8)) \\ &= \frac{9.8 \text{ ms}^{-2}}{185 \text{ K}}(8.07 \text{ K/km}) \\ &= \frac{9.8 \text{ ms}^{-2}}{185 \text{ K}}(\frac{8.07 \text{ K}}{1000 \text{ m}}) \\ &= 0.0004 \text{ s}^{-2}\end{aligned}$$

therefore

$$\omega_B = 0.021 \text{ s}^{-1}$$

Hence, the minimum period of AGWs in mesosphere can be calculated in the form (i.e. Brunt-Väisälä period):

$$\tau = \frac{2\pi}{\omega_B} = \frac{2\pi}{0.017} = 5 \text{ minutes}$$

2.4 Dispersion Relation for AGWs

When atmospheric gravity waves travel through a stable and motionless atmosphere, the first order perturbation is considered. Ignoring viscosity, the perturbation of pressure, velocity and density are given by the following [Hines, 1960]:

$$P = P_0 e^{i(wt - K_x x - K_z z)} \tag{2.17}$$

$$\rho = \rho_0 e^{i(wt - K_x x - K_z z)} \tag{2.18}$$

$$U_x = U_{0x} e^{i(wt - K_x x - K_z z)} \tag{2.19}$$

$$U_z = U_{0z} e^{i(wt - K_x x - k_z z),} \tag{2.20}$$

where U_x and U_z are horizontal and vertical velocity components of the perturbation, ω is the angular frequency of the AGW, K_x is a horizontal wave number while K_z is the vertical wave number.

Substituting equations 2.17 - 2.20 in the adiabatic equation, equation of motion and the continuity equation gives [Hines, 1960; Beer, 1978; Nappo, 2013]:

$$\frac{\partial \rho}{\partial t} + U \cdot \nabla \rho_0 + \rho_0 \nabla \cdot U = 0. \tag{2.21}$$

Because horizontal motions are independent of the gravity, therefore the equation of motion along the horizontal motion and the vertical motion can be written in the form, respectively:

$$\rho_0 \frac{\partial U_x}{\partial t} + \frac{\partial P}{\partial x} = 0 \tag{2.22}$$

$$\rho_0 \frac{\partial U_z}{\partial t} + \frac{\partial P}{\partial z} + \rho g = 0 \tag{2.23}$$

$$\frac{\partial P}{\partial t} + U \cdot \nabla P_0 - c_s^2 \frac{\partial \rho}{\partial t} - c_s^2 U \cdot \nabla \rho_0 = 0, \tag{2.24}$$

where

$$c_s^2 = \gamma \frac{P_0}{\rho_0} \tag{2.25}$$

c_s is the speed of sound and γ is the ratio of specific heats at constant pressure and volume [Kelley, 2009]. In section 2.3 it is shown that the mesosphere is unstable, thus for small

change in z, the density of an atmosphere decreases with altitude Nappo [2013]. Therefore the unperturbed density along vertical motion can be written in the form [Hines & Hines, 1974]:

$$\rho_0(z) \propto e^{-\frac{z}{H}}. \tag{2.26}$$

where H is the scale height and z is measured vertical displacement. Now substituting equations 2.18 and 2.26 into equation 2.21 results in the following terms:
First term:

$$\frac{\partial \rho}{\partial t} = \frac{\partial}{\partial t}(\rho_0 e^{i(\omega t - K_x x - K_z z)}) = -i\omega e^{i(\omega t - K_x x - K_z z)} \tag{2.27}$$

$$\frac{\partial \rho}{\partial t} = i\omega\rho \tag{2.28}$$

Second term:

$$U \cdot \nabla \rho_0 = U\left(\frac{\partial}{\partial x} + \frac{\partial}{\partial z}\right)\left(e^{-\frac{z}{H}}\right) = -\frac{U_z \rho_0}{H} \tag{2.29}$$

Third term:

$$\rho_0 \nabla \cdot U = \rho_0\left(\frac{\partial}{\partial x} + \frac{\partial}{\partial z}\right)\left(U_{(x,z)_0} e^{i(\omega t - K_x x - K_z z)}\right) \tag{2.30}$$

$$\rho_0 \nabla \cdot U = \rho_0[-iK_x U_x - iK_z U_z] \tag{2.31}$$

adding all the terms yields

$$i\omega\rho - \frac{U_z \rho_0}{H} - \rho_0 i K_z U_z - \rho_0 i K_x U_x = 0. \tag{2.32}$$

Multiplying by $1/\rho_0$, equation 2.32 takes the form

$$i\omega\frac{\rho}{\rho_0} - \frac{U_z}{H} - iK_z U_z - iK_x U_x = 0 \tag{2.33}$$

$$i\omega\frac{\rho}{\rho_0} - iU_x K_x - \left(\frac{1}{H} + iK_z\right)U_z = 0. \tag{2.34}$$

Substituting equation 2.17 and equation 2.19 into equation 2.22, gives

$$\rho_0 \frac{\partial}{\partial t}\left(\mathrm{U}_{0x} e^{i(\omega t - K_x x - K_z z)}\right) + \frac{\partial}{\partial x}\left(P_0 e^{i(\omega t - K_x x - K_z z)}\right) = 0 \tag{2.35}$$

$$i\rho_0 \omega U_x - iK_x P = 0. \tag{2.36}$$

Dividing both sides by P_0 yields

$$i\frac{\rho_0}{P_0}\omega U_x - iK_x\frac{P}{P_0} = 0. \tag{2.37}$$

Using equation 2.25, the above equation can be written as:

$$-iK_x\frac{P}{P_0} + i\frac{\gamma}{c_s^2}\omega U_x = 0 \tag{2.38}$$

$$-\frac{c_s^2 K_x}{\gamma}\frac{P}{P_0} + \omega U_x = 0. \tag{2.39}$$

Now substituting equation 2.17 and 2.20 into equation 2.23

$$\rho\frac{\partial}{\partial t}\left(U_{0z}e^{i(\omega t - K_x x - K_z z)}\right) + \frac{\partial}{\partial z}\left(P_0 e^{i(\omega t - K_x x - K_z z)}\right) + \rho g = 0 \tag{2.40}$$

$$i\omega U_z\rho_0 + e^{i(\omega t - K_x x - K_z z)}\frac{\partial P_0}{\partial z} - iK_z P_0 e^{i(\omega t - K_x x - K_z z)} + \rho g = 0 \tag{2.41}$$

$$i\omega U_z + \frac{1}{\rho_0}e^{i(\omega t - K_x x - K_z z)}\frac{\partial P_0}{\partial z} - iK_z\frac{P_0}{\rho_0}e^{i(\omega t - K_x x - K_z z)} + \frac{\rho}{\rho_0}g = 0. \tag{2.42}$$

Since

$$H = \frac{c_s^2}{\gamma g} \tag{2.43}$$

and from the hydrostatic equilibrium theory

$$\frac{\partial P_0}{\partial z} = -\rho_0 g, \tag{2.44}$$

thus equation 2.42 can be written as

$$i\omega U_z - \frac{1}{\rho_0}\rho_0 g e^{i(\omega t - K_x x - K_z z)} - iK_z\frac{c_s^2}{\gamma}e^{i(\omega t - K_x x - K_z z)} + \frac{\rho}{\rho_0}g = 0 \tag{2.45}$$

$$i\omega U_z - \frac{c_s^2}{\gamma H}e^{i(\omega t - K_x x - K_z z)} - iK_z\frac{c_s^2}{\gamma}e^{i(\omega t - K_x x - K_z z)} + \frac{\rho}{\rho_0}g = 0. \tag{2.46}$$

Equation 2.46 can be written in the form

$$g\frac{\rho}{\rho_0} - \left(\frac{c_s^2}{\gamma H} + i\frac{K_z c_s^2}{\gamma}\right)\frac{P}{P_0} + i\omega U_z = 0 \tag{2.47}$$

$$g\frac{\rho}{\rho_0} - \left(\frac{1}{H} + iK_z\right)\frac{C_S^2}{\gamma}\frac{P}{P_0} + i\omega U_z = 0, \tag{2.48}$$

where $\frac{P}{P_0} = e^{i(\omega t - K_x x - K_z z).}$

Equation 2.24 reduces to

$$\frac{\partial}{\partial t}\left(P_0 e^{i(\omega t - K_x X - K_z Z)}\right) + U \cdot \frac{\partial \mathrm{P}_0}{\partial z} - c_s^2 \frac{\partial}{\partial z}\left(\rho_0 e^{i(\omega t - K_x X - K_z Z)}\right) - c_s^2 U \cdot \frac{\partial \rho_0}{\partial z} = 0, \tag{2.49}$$

$$i\omega P + U_z(-\rho_0 g) - c_s^2(i\omega\rho) + c_s^2 U_z \cdot \frac{\rho_0}{H} = 0, \tag{2.50}$$

$$i\omega P - U_z \frac{c_s^2}{\gamma H}\rho_0 - i\omega c_s^2 \rho + c_s^2 U_z \frac{\rho_0}{H} = 0. \tag{2.51}$$

Grouping the like terms gives us

$$i\omega P - i\omega c_s^2 \rho - (1-\gamma)\frac{\mathrm{c}_s^2 \rho_0}{\gamma H} U_z = 0, \tag{2.52}$$

and multiplying by $1/\rho_0$

$$i\omega \frac{P}{\rho_0} - i\omega s_s^2 \frac{\rho}{\rho_0} + (\gamma - 1)\frac{c_s^2}{\gamma H}\mathrm{U}_z = 0. \tag{2.53}$$

Using equation 2.25, the above equation infers that

$$i\frac{\omega c_s^2}{\gamma}\frac{P}{P_0} - i\omega c_s^2 \frac{\rho}{\rho_0} + (\gamma - 1)\frac{c_s^2}{\gamma H} U_z = 0. \tag{2.54}$$

Let $\vec{F}$ be a vector such that

$$\vec{F} = \begin{pmatrix} \frac{\rho}{\rho_0} \\ \frac{P}{P_0} \\ U_x \\ U_z \end{pmatrix} \tag{2.55}$$

Now writing equations 2.34, 2.38, 2.48 and 2.54 in the matrix form, deduce that

$$\begin{pmatrix} i\omega & 0 & iK_x & -(1/H + iK_z) \\ 0 & -\frac{iK_x c_s^2}{\gamma} & i\omega & 0 \\ g & -(1/H + iK_z)\frac{c_s^2}{\gamma} & 0 & i\omega \\ -i\omega c_s^2 & \frac{i\omega c_s^2}{\gamma} & 0 & (\gamma - 1)\frac{c_s^2}{\gamma H} \end{pmatrix} \begin{pmatrix} \frac{\rho}{\rho_0} \\ \frac{\mathrm{P}}{\mathrm{P}_0} \\ \mathrm{U}_x \\ \mathrm{U}_z \end{pmatrix} \tag{2.56}$$

Letting the determinant of the matrix to be zero such that the solution of this matrix is non-trivial. Therefore the solution of the matrix is given in the form [Hines, 1960]:

$$\omega^4 - \omega^2 c_s^2(K_x^2 + K_z^2) + (\gamma - 1)g^2 K_x^2 + ig\gamma\omega^2 K_z = 0. \tag{2.57}$$

Assuming further that the wave amplitude remain constant in the horizontal direction, concludes that $K_x = k_x$, where k_x is real. In the vertical amplitude $K_z = k_z + ik_z'$ with k_z and k_z' real and imaginary amplitudes respectively. Now substituting this transforming equations into equation 2.57, gives

$$\omega^4 - \omega^2 c_s^2(k_x^2 - k_z'^2 + k_z^2 + 2ik_z k_z') + (\gamma - 1)g^2 \mathrm{k}_x^2 + ig\gamma\omega^2 k_z - g\gamma w^2 k_z' = 0. \tag{2.58}$$

Separating the real part and the imaginary part from the complex solution, deduce:

$$\omega^4 - \omega^2 c_s^2(k_x^2 - k_z'^2 + k_z^2) + (\gamma - 1)g^2 k_x^2 - g\gamma\omega^2 k_z' = 0, \tag{2.59}$$

and

$$-\omega^2 c_s^2(2ik_z k_z') + ig\gamma\omega^2 k_z = 0. \tag{2.60}$$

Dividing both sides by i and factoring out $\omega^2 \mathrm{k}_z$ equation 2.60 reduces to

$$w^2 k_z(\gamma g - 2c_s^2 k_z') = 0.$$

For this equation to hold, one of these conditions must be true:

$$w^2 k_z = 0 \quad \cup \quad \gamma g - 2c_s^2 k_z' = 0.$$

These conditions are valid only if one of the following is true:

$$\omega = 0, \tag{2.61}$$

$$k_z = 0, \tag{2.62}$$

$$k_z' = \frac{\gamma g}{2c_s^2}. \tag{2.63}$$

The desired condition is equation 2.63 because equation 2.61 shows that there exists no wave as there is no period or velocity implying that the wave is stationary, and equation 2.62 implies that the wave only propagates horizontally.

Now taking the condition $k_z' = \frac{\gamma g}{2c_s^2}$ and substituting it into equation 2.57 results in:

$$\omega^4 - \omega^2 c_s^2(k_x^2 + k_z^2) + (\gamma - 1)g^2 k_x^2 - \omega^2 g^2 \frac{\gamma^2}{4c_s^2} = 0. \tag{2.64}$$

Equation 2.64 is the dispersion relation for AGWs [Hines, 1960]. Let the minimum frequency for sound waves be w_a, such that $w_a = \frac{\gamma g}{2c_s}$, equation 2.64 then reduces to

$$\omega^4 - \omega^2 c_s^2(k_x^2 + k_z^2) + (\gamma - 1)g^2 k_x^2 - \omega^2 \omega_a^2 = 0. \tag{2.65}$$

The Brunt-Väisälä frequency in terms of speed of sound and scale height is given by equation [Hines & Hines, 1974]:

$$\omega_B^2 = \left(\gamma - 1 + \gamma \frac{dH}{dz}\right) \frac{g^2}{c_s^2}\ , \tag{2.66}$$

which is the maximum possible frequency of the disturbed air parcel. This is referred to as the atmospheric gravity wave, which is the oscillation of air in response to buoyancy [Hines, 1960; Nappo, 2013]. Because the scale height is constant thus

$$\frac{dH}{dz} = 0$$

This implies that equation 2.66 reduces to

$$\omega_B^2 = (\gamma - 1)\, \frac{g^2}{c_s^2}. \tag{2.67}$$

Making k_z^2 the subject of the formula in equation 2.65 and using equation 2.67 yields

$$k_z^2 = \left(\frac{\omega_B^2 - \omega^2}{\omega^2}\right) k_x^2 + \frac{1}{c_s^2}\left(\omega^2 - \omega_a^2\right). \tag{2.68}$$

If $\omega >> (\omega_B; \omega_a)$, then

$$k_z^2 \approx \frac{\omega^2}{c_s^2} - k_x^2 \Rightarrow k_z^2 + k_x^2 \approx \frac{\omega^2}{c_s^2}. \tag{2.69}$$

Which means that the wave is a sound wave, and have periods less than 4 minutes in the atmosphere [Beer, 1974].

At low frequencies i.e $\omega << (\omega_B; \omega_a)$, then

$$k_z^2 \approx \frac{\omega_B^2}{\omega^2} k_x^2 - \frac{\omega_a^2}{c_s^2} \tag{2.70}$$

This represents the propagation of a wave that is under the influence of gravity. In the atmosphere AGWs propagate with periods between 4 minutes and 3 hours [Beer, 1974].

2.5 Sources of gravity waves

The AGWs are generally created in the troposhere and are usually a result of the weather and topographic phenomenon such as wind that blows over the mountains and some are created by thunderstorms. Natural disasters such as volcanic eruptions and earth quakes, are phenomena that can generate AGWs [Hines, 1960; Afraimovich et al., 2001; D. C. Fritts & Alexander, 2003]. Other sources of AGWs include meteorites, auroral activity, solar eclipses as well as man made sources such as nuclear explosions and rocket launches [Naero, 2013; Bakken, 2015].

Abrupt changes in the pressure and temperature of the atmosphere result in the boundary between day and night-time known as the solar terminator. A similar boundary is also oberved during a solar eclipse [Rishbeth, 1968; Somsikov & Ganguly, 1995]. These abrupt changes cause instabilities in the pressure. A gravity force is in turn induced, that forces the atmospheric gravity waves to propagate in the same direction (mainly westward) as the solar terminator [Somsikov & Trotskii, 1975]. During geomagnetic storms AGWs can be found traveling poleward as well as equatorward, although equatorward AGWs have Joule heating and particle precipitation as other mechanisms through which they can be generated. Poleward AGWs during geomagnetic storms are generated by equatorial electrojet and increased Lorentz coupling [Thome, 1968; Chimonas, 1970; Hernandez & Roble, 1978; Habarulema et al., 2015, 2018].

2.6 Modes of Atmospheric gravity wave propagation

There are multiple modes of AGW propagation, including freely propagating upwards or downwards, ducted propagation of trapped waves, as well as secondary and tertiary waves [Walterscheid et al., 2001]. The four main modes that atmospheric gravity waves can take up as they move in the atmosphere were shown by Mayr et al. [1991] which rely on the magnitude and source of the waves. As seen in Figure 2.3, the AGWs in mode (1) in the thermosphere move almost horizontally. The characteristics related to these waves are that they travel at high speeds for greater distances and have longer wavelengths and mostly found in the thermosphere. It was Hocke et al. [1996] who pointed out that these waves propagate equatorward which is a characteristic related to waves that originate from higher latitudes at the inception of geomagnetic storms. The atmospheric gravity waves generated in the lower thermosphere are depicted in mode 2. They travel at diagonal angles relative to the Earth's surface, have short

wavelengths and because there is high viscosity and thermal conduction at upper atmospheric regions, these waves dissipate quickly as they travel upwards [Hines, 1964; Kohl et al., 1996].

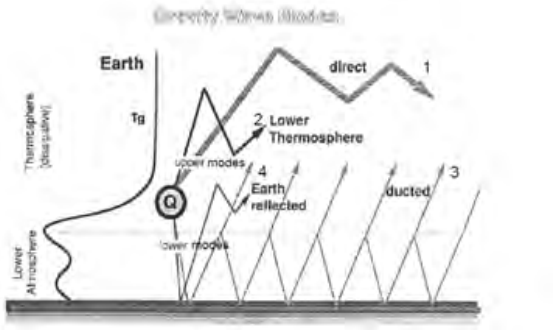

Figure 2.3: Atmospheric gravity wave modes in the lower and upper atmosphere [Mayr et al., 1991]

A wave travelling between the Earth's surface and the lower thermosphere is represented by mode 3. This type of wave even though it can leak into the upper atmosphere, is able to travel for longer distances due to its minimal viscosity and thermal conduction in the lower atmosphere. Mode 4 represents those waves that are reflected on the Earth's surface and travel into the thermosphere [Beer, 1974; Hajkowicz, 1990; Francis, 1974]. The AGWs in modes 3 and 4 travel at low speeds and have short wavelengths. These gravity waves do not have much of an impact in atmospheric processes due to their random occurrence [Beer, 1974; Hajkowicz, 1990; Francis, 1974].

Chapter 3

Instrument and Data analysis

In this chapter the instrument, which is the airglow imager, is discussed followed by how it was used to determine parameters of the atmospheric gravity waves. Before the gravity wave parameters could be determined, a three-step approach has been employed using the MATLAB programming language. First, the airglow images went through coordinate mapping, secondly star removal was done, which included filtering. The stars were removed because they serve as noise, resulting in streaking of the image when it is projected to geographic coordinates or when averaged for flat fielding. Third, through a process known as unwarping, the image is transformed to a uniformly spaced geographical coordinate system. Last, spectral analysis was performed in order to calculate gravity wave characteristics.

3.1 All-sky Imager

The all sky imager (see figure 3.1) used in this study was designed and is operated by Boston University. This instrument deployed at Sutherland, South Africa (32.37°S, 20.81°E, magnetic latitude: 40.7°S) utilizes an 85 mm fisheye lens with a 180 degrees field of view to record the scene from horizon to horizon at all azimuths. It uses a highly-efficient 1024 x 1024 pixel back illuminated charged coupled device (CCD) detector. The system houses six filters with a narrow band 1.2 – 1.8 nm full width half maximum in its filter wheel. Some of the filters housed in the filter wheel are assigned the characteristics seen in table 3.1.

Table 3.1: Different airglow emissions and their specific characteristics [Makela et al., 2001; Chattopadhyay & Midya, 2006].

Species	Wavelength	Emission height	Layer thickness
OI	630.0 nm	250 km	50 km
OI	557.7 nm	96 km	15 km
Na	589.3 nm	90 km	7 km
OI	777.4 nm	350 km	50 km
OH	845.0 nm	87 km	10 km

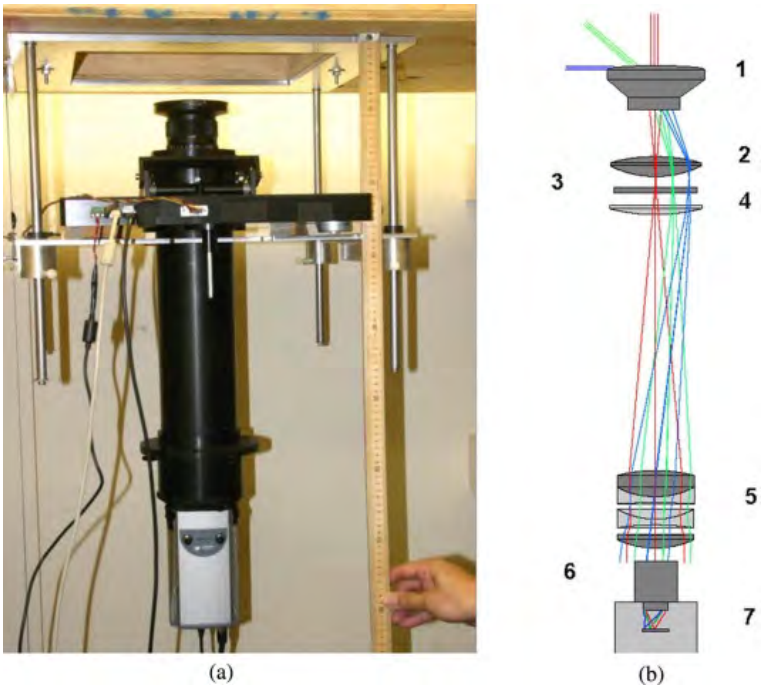

Figure 3.1: All-sky imager (ASI) designed at Boston University for observations of emissions from the Earth's upper atmosphere [Martinis et al., 2018]

There exists also one filter which is centered at 605.0 nm that has no emission lines, that is used to assess the presence of tropospheric clouds and background light, and the cutoff filter of $>$ 695.0 nm [Hickey et al., 2018]. The integration times are 2 min resulting in a sequence of images at given wavelength separated by approximately 11 min. In addition, the 605 nm filter is used

because there are no airglow emission lines within the bandwidth of the filter. Any emissions within the 605 nm filter passband is due to either the stellar continuum or weak broadband airglow. It can therefore be used to remove any background emission within the bandpass of the other filters. [Martinis & Mendillo, 2007; Martinis et al., 2013, 2018, 2019]. The raw data from this instrument is streamed to Boston University and the images are published on their website: http://Sirius.bu.edu/data. The airglow imaging technique has been used for studies of mesospheric bores [Taylor et al., 1995; S. Smith et al., 2005; Nielsen et al., 2006; Mondal et al., 2019], gravity waves [F. Garcia et al., 1997; D. C. Fritts & Alexander, 2003; Taylor et al., 2009], traveling ionospheric disturbancess [Mendillo et al., 1997; Shiokawa et al., 2003; Martinis et al., 2019] and plasma bubbles [Takahashi et al., 2009; Taori et al., 2015; Takahashi et al., 2018]. The next section presents how the raw data from this instrument are processed.

3.2 Image Processing

To make sense of the acquired airglow images, some image processing techniques have to be applied to the airglow images. The processing is done to convert the airglow images from pixel coordinate system to an easier to understand system, such as the geographical coordinate system. There are characteristics of the raw image that need to be preserved, such as gravity waves, and those that need to be removed, such as stars. This can be achieved through filtering.

3.2.1 Preprocessing

Before the preprocessing can be done, the gravity wave images were first manually inspected for gravity wave features. These are wavelike patterns of bright and dark bands seen on the image as illustrated by the bottom right image in figure 3.2. The aim of the preprocessing is to unify the resolution across the images, to transform the images from all-sky format to the corresponding geographic coordinate system followed by the removal of stars and end with unwarping. The two methods used to analyse the Sutherland airglow data were visual inspection of the images available on the Boston University data website (http://Sirius.bu.edu/data) and spectral analysis. The visual inspection included identification of dates containing data by how the calendar dates are highlighted on the website with a red colour for dates when the data are available while those without data are grey. The next step involved identification of nights with

good data coverage (i.e. without or very little cloud coverage) and followed by the identification of those with AGW signatures. Having identified the relevant airglow images, spectral analysis was used to determine the gravity wave parameters such as horizontal wavelength, phase speed, propagation direction, and period.

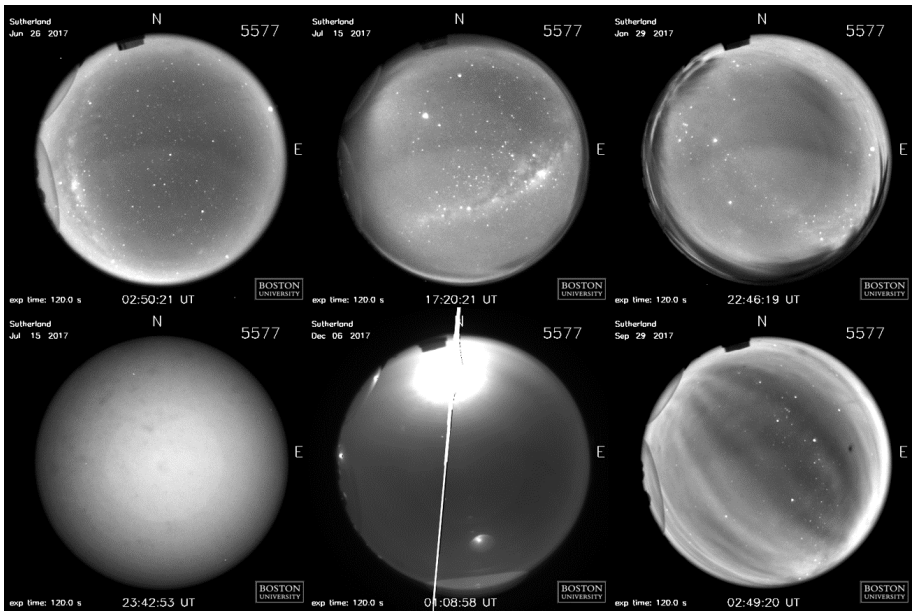

Figure 3.2: The images illustrate from top left, clear, mostly clear, mostly cloudy, completely cloudy, moonlight contamination and AGW signatures.

Although the airglow imager in Sutherland started collecting data from June of 2016, this study used OI 557.7 nm airglow data taken during January − December 2017. This period was chosen to allow sufficient data to perform seasonal analysis of the calculated wave parameters. The images are taken between sunset and sunrise, roughly between 16:00 UT and 04:00 UT (where LT hour = UT + 1.65) although these vary with season. Some of the dates in 2017 did not have data and this could be because of camera maintenance or malfunction, so out of 365 nights data were available for only 323 nights. The data were sorted from those with cloud and moon appearances resulting with 206 clear nights. Those used were clear or mostly clear and those that were mostly clear were included as they were clear enough for airglow features to be observed in the presence of clouds. To declare a night as being clear or unclear, we used the visibility of stars in the images throughout the night. A night was declared to be unclear when stars were not visible in all or most of the images of that night's observation, due to cloud cover or moonlight contamination. The amount of clear images and cloudy images varies

throughout the data. Figure 3.2 illustrates the different classification of images, namely clear (top left), mostly clear (top middle), mostly cloudy (top right), completely cloudy (bottom left), moonlight contamination (bottom middle) and lastly AGW signatures (bottom right). Note AGW event was defined as a wave-like pattern that is observed in airglow images which last for at least 3 successive images (i.e. for 33 minutes) with most of its features preserved (i.e. not changing drastically). Most of the events last for less than an hour, with only a few cases where events last for a few hours. Once the images with AGW features were identified, a coordinate mapping procedure was applied to them as described in the section below.

Mapping to geographical coordinates

Figure 3.3 shows the mapping sequence used to transform all-sky images from the pixel coordinate system to geographic coordinates. The original image (see figure 3.3 top left) shows the image data array with the indices represented by pixel coordinates (i,j). The standard coordinate system is defined such that the centre corresponds with the zenith and the scaling of the coordinates result in the horizon circle corresponding to 0° elevation in units of radius. Every pixel coordinate (i,j) of the original image corresponds to a standard coordinate (f,g). The elevation-azimuth coordinate system makes it easier to transition between the standard coordinates and geographic coordinates. The desired coordinate system is the geographic coordinate system where the standard coordinate system is mapped to points (x,y) through the azimuth and elevation transformation.

The distortion effect observed in airglow images by which the image appears compressed and curved towards the horizon is a result of a fish-eye lens which gives incorrect gravity wave wavelength values if not corrected. Figure 3.4 illustrates the airglow geometry, where point P is the sky position of the object of interest, O is the station where the observer is based, R is the mean radius of the Earth, H is the altitude of the peak emission layer, el is the elevation over the horizon, Ψ is the angle of P from zenith referenced from the centre of the Earth, r is the geographical distance between zenith and point P, a the distance between zenith and point P, c is the distance between the station and point P and α is the angle between the station and the zenith point.

The relationship between the parameters, shown in Figure 3.3 and Figure 3.4, is given by the following equations:

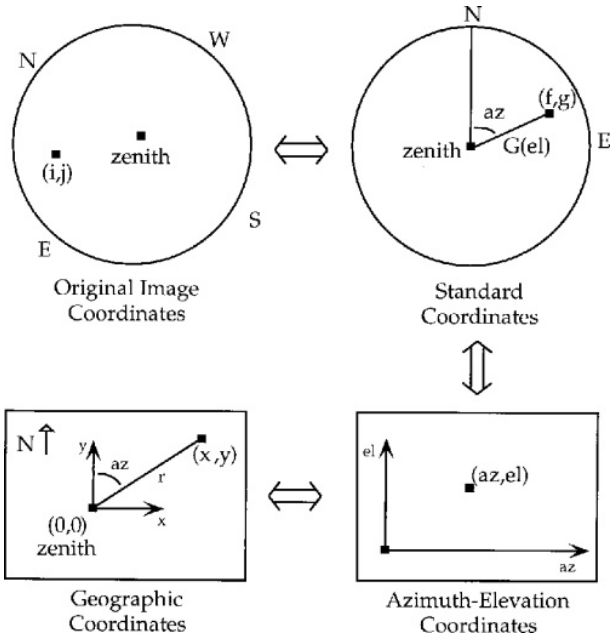

Figure 3.3: Coordinate mappings used to transform all-sky images to desired coordinate system [F. Garcia et al., 1997].

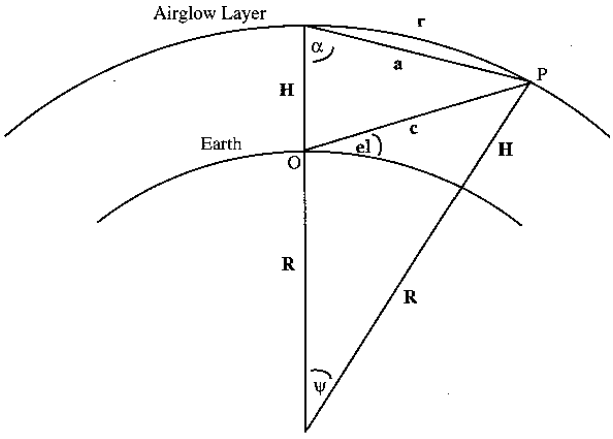

Figure 3.4: Illustration of the airglow geometry [F. Garcia et al., 1997].

$$r = \sqrt{x^2 + y^2} \tag{3.1}$$

$$\psi = \frac{r}{R + H} \tag{3.2}$$

$$a = 2(R + H)sin\frac{\psi}{2} \tag{3.3}$$

$$c = \sqrt{(H^2 + a^2 - 2Hacos(\alpha))} \tag{3.4}$$

$$\alpha = (\frac{\pi - \psi}{2}) \tag{3.5}$$

$$el = cos^{-1}\left(\frac{asin\alpha}{c}\right) \tag{3.6}$$

where R is the mean radius of the Earth (6370 km) and the angle it makes with the y axis gives the azimuth at any point (x,y) in the geographic coordinate system is given by:

$$az = tan^{-1}\left(\frac{x}{y}\right). \tag{3.7}$$

The propagation direction of the waves can be accurately estimated once the data has a geographic reference system. The first step in this regard is to find the zenith and polar star in order to find the true north. The zenith is not necessarily located in the center of the image which makes it necessary to find its location using other means. This can be done during the mapping to geographical coordinates which utilizes a star map to compare the positions of the stars in the image with their theoretical locations. Mapping to geographical coordinates eliminates the effects caused by the curvature of the night sky being studied where the pixels at the boundary of the image cover a larger area than those in the middle [Hatlen, 2013]. Figure 3.5 shows the raw image in pixel coordinates (left) and geographic coordinates (right).

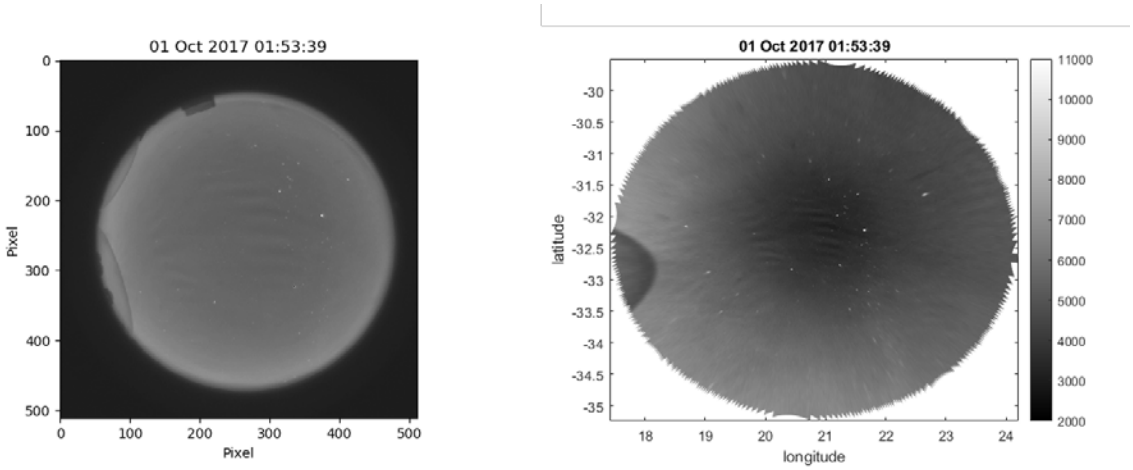

Figure 3.5: The raw image in pixel coordinates and geographic coordinates.

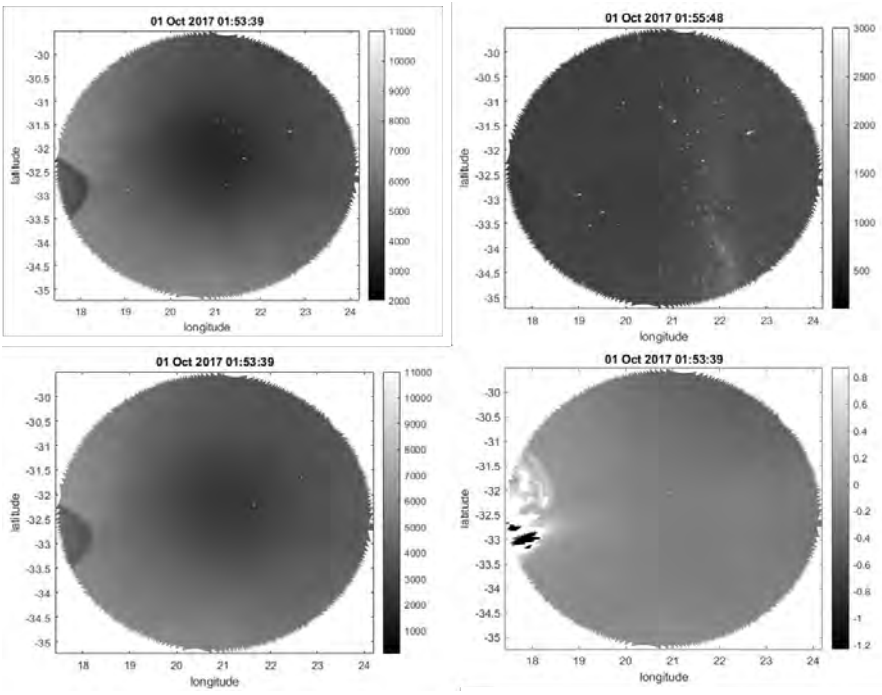

Figure 3.6: Illustration showing the original image (top left), background image (top right), image after background subtraction (bottom left) and filtered image (bottom right).

Star removal

It is important to remove the stars in an airglow image because they can cause streaking when the image is projected onto a geographic coordinates system as well as act as noise in the image when calculating the gravity wave parameters [F. Garcia et al., 1997]. Stars show up in the raw images as bright spots of varying sizes as seen in figures 3.2, 3.5 and 3.6 for example. They have an intensity that is greater than that of the background radiation and the wave crests as a result of the gravity waves propagating through the airglow layers. It is hard and almost impossible to remove stars by just subtracting two subsequent images from the same wavelength filter. Therefore the star removal was done by first subtracting the background using the images from the 605.0 nm wavelength (example given in 3.6 top right) then applying a median filter. Images from 605.0 nm are used because they have the same exposure time and are taken in close succession as those from the 557.7 nm wavelength (example given in 3.6 top left). This removes the background and it allows the wave crests to be easily detectable (as illustrated by 3.6 bottom left).

After removing the background the 557.7 nm images are filtered using the median filter provided

by MATLAB at either a 5x5 or 10x10 pixel window. The median filter sorts out what is referred to as the salt and pepper noise in images. As a ranking filter it replaces the noise with the median intensity value of the data within the filter window.The window size needs to be large enough to be able to remove most of the stars if not all of them. The process results in an image similar to that illustrated by the bottom right image in Figure 3.6 with a re-scaled grey scale. The image shows the linear variation of fractional intensity of the image. The positive values corresponding to the lightest intensity values and negative values corresponding to the darkest intensity values which are a result of the image subtraction.

3.2.2 Unwarping

The image was transformed from geographic coordinates to distance coordinates, a procedure also known as unwarping, so that it could be analysed using standard spectral analysis. An area of the image where the gravity wave appears is isolated for analysis as illustrated by the left plot of figure 3.7. The selected region was plotted on latitude and longitude scale and the white space was removed to make the image square by linear extrapolation over the area of interest. The rectangular image was converted from latitude and longitude coordinates to distance in kilometers as seen in figure 3.7 (right) at an assumed altitude of 96 km.

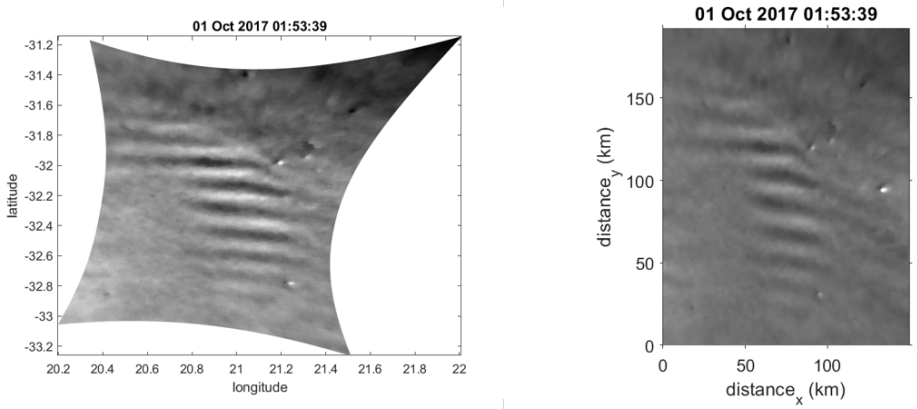

Figure 3.7: Isolated area where gravity wave structure is seen and the transformed image with distance coordinates

.

3.3 Data Analysis

The method employed in this project was specifically designed to place emphasis on the regions of interest (i.e. where AGWs appear in images) making it easier to focus on the events present and apply spectral analysis to determine wave parameters.

3.3.1 Wavelength

The method used in this study to determine wavelength, referred to as the propagation vector method, required that two consecutive images showing AGW features have the same dimensions. Using the Ginput MATLAB function the line joining two points which encompasses the wavefronts of the wave, called the propagation vector, was selected on the first image. This line, seen in figure 3.8, is superimposed onto the next image. The wavelength for each image was obtained along the propagation vector perpendicular to the wavefronts.

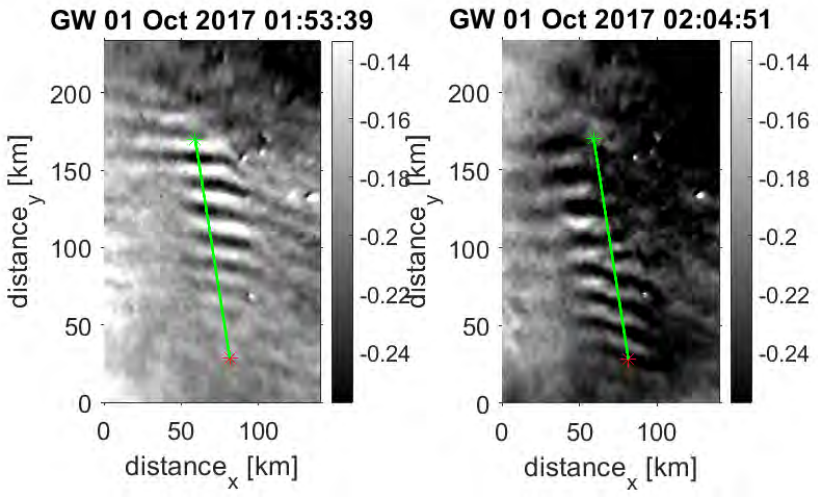

Figure 3.8: Two images from different time stamps shown side by side and the line drawn using the propagation vector method is shown in both images.

The left column of figure 3.9 was obtained by extracting the intensity variation along the propagation vector in figure 3.8 and the plots on the right in figure 3.9 are the 1D Fourier transforms of the plots on the left.

Two methods were available for determining the wavelength:

1. 'auto' wavelength selection - for this method the peaks of the 1D Fourier transform of the

waves along the selected path were used to determine the dominant ("mean") wavelength. The peak of the Fourier transform gives the average wave number. The part of the wave that is then highlighted is the crest-to-crest section which has a distance between crests that is closest to the wavelengths determined from the Fourier transform.

2. 'manual' wavelength selection - this method prompts the user to pick two successive crests from each of the 1D waves shown in figure 3.9, which by manual inspection seems to be the clearest "cycle" of the respective waves. In each of the images the wavelength was then taken as the distance between the selected successive crests. In this case the 1D Fourier transform was not used for finding the wavelength, but nevertheless determined, and marked with an asterisk at the location of the wavelength determined by the crests selected from P1 and P2 waves.

Using the auto method to find the wavelength, the one-dimensional wave analysis of figure 3.8 was obtained by deriving the wave amplitude along the selected propagation vector as seen in figure 3.9. The pixel intensity values along the velocity vector were found and the velocity vectors was interpolated to 512 points so that the Fast Fourier Transform (FFT) function can give a meaningful frequency response, and plot the points along the same propagation vector on each of the two images.

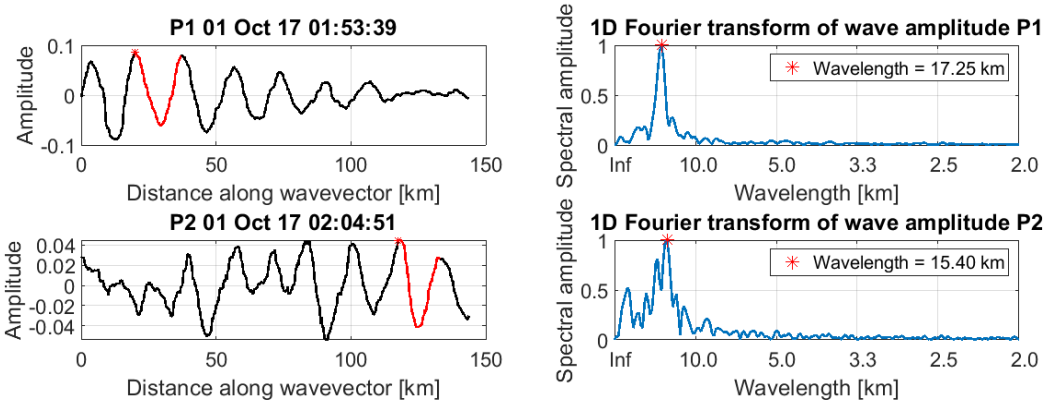

Figure 3.9: 1D Fourier transform of wave amplitude.

3.3.2 Velocity

The velocity of the AGW was calculated using cross-correlation of the intensity variation extracted from the propagation vector of the two consecutive images of the same event (see left

plot of figure 3.10). The velocity calculated to be 10.04 m/s was determined by the highest peak of the 1D correlation as this shows the maximum correlation found between the two waves (see figure 3.10 plot on the right). The possible velocities shown for selection are those corresponding to the peaks of the cross correlation plot which are set to a range between 10 and 100 m/s as identified by Nakamura et al. [1999] and Essien et al. [2018] to be the typical range of the velocities of small scale waves and can be adjusted for other types of gravity wave scales. The distance between the blue and red triangle is the distance the wave has travelled between snapshots and not its wavelength.

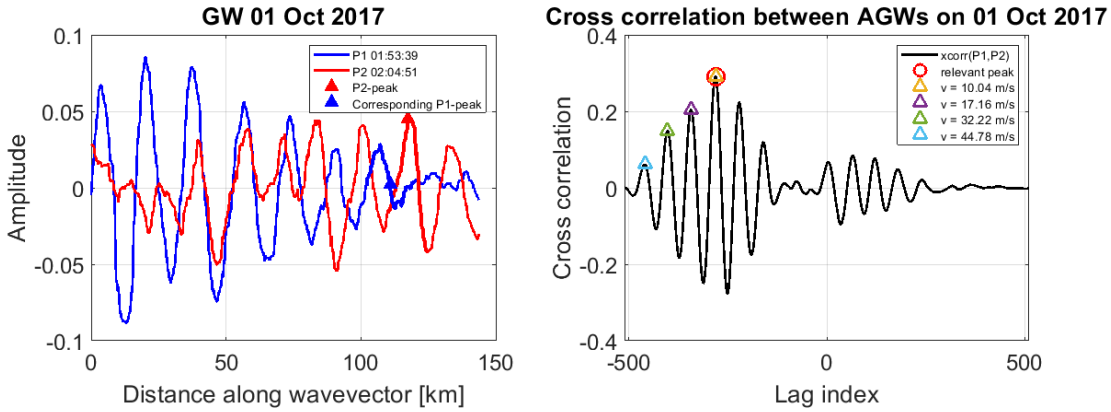

Figure 3.10: Plot of the cross correlation.

3.3.3 Period

Having determined the wavelength and the phase speeds of the gravity waves, the period of the wave is simply calculated from the equation

$$P = \frac{\lambda}{V} \tag{3.8}$$

where the P is period, λ represents the wavelength in kilometres (km) and V is the phase speed in m/s.

Chapter 4

Results and Discussion

The identified images with clear gravity waves were analyzed and in some instances, more than one wave event was observed on the same set of successive images. A total of 323 nights had airglow observations, from which only 206 nights had clear visibility conditions, and out of those gravity waves were detected in only 49 nights. A total of 53 wave events were observed as shown in Table 4.1. Note that for some of the events only their wavelengths could be calculated as they were observed in only one image. Table 4.1 shows that the wavelengths range between 11 and 85 km, velocity between 9 and 82 m/s, periods are from 4 to 50 minutes and the propagation azimuths range between 11 and 344 °. Note that one of the AGWs have a period less than the BV period determined in Chapter 2. The BV period was calculated based on global statistical estimates of mesospheric conditions. Also there'll be some error in the estimate of period associated with signal processing methods used. Therefore, it is expected that there'll be a small difference between the BV period and the minimum period determined from observations as evident in the results presented in Table 4.1.

Some waves structures exhibit the characteristics of ripples by their short horizontal wavelengths (generally $< \sim 15$ km) and their low horizontal velocities (generally $< \sim 10$ - 15 m/s) [Taylor & Hapgood, 1990; Hecht, 2004]. Ripple-type waves are due to instabilitites in the local medium and do not propagate vertically [Hecht, 2004; Nakamura et al., 1999]. The phenomenon is beyond the scope of this project and therefore is not considered further.

The months of the year were assigned to a season as seen in Table 4.2 similarly to those selected by Parkinson et al. [2001] and Matamba et al. [2015]. This makes it possible to observe seasonal variations for the gravity wave activity.

Table 4.1: Observed parameters of AGWs at Sutherland, South Africa in 2017.

Date	Events	Time interval (UT)	wavelength (km)	Azimuth (°)	Velocity (m/s)	Period (min)
16 Jan 2017	1	20:04 - 20:38	33	172	81	6
18 Jan 2017	2	21:33 - 22:07	27	157	61	18
24 Jan 2017	3	20:23 - 21.08	35	147	47	28
26 Jan 2017	4	22:14 - 22:14	14			
30 Jan 2017	5	02:04 - 02:27	22	124	30	10
01 Feb 2017	6	21:58 - 22:21	27	148	62	8
04 Feb 2017	7	00:01 - 00:35	30	178	40	17
	8	00:01 - 00:57	24	143	37	11
20 Feb 2017	9	19:01 - 19:24	18	11	45	7
23 Feb 2017	10	20:50 - 21:35	37	136	39	16
24 Feb 2017	11	01:52 - 02:48	14	149	36	6
27 Feb 2017	12	22:49 - 23:00	22	139	31	12
02 Mar 2017	13	00:11 -00:33	14	149	36	14
17 Mar 2017	14	18:52 - 19:48	28	19	58	8
02 Apr 2017	15	00:46 - 01:31	25	228	82	5
03 Apr 2017	16	22:49 - 23:11	15	167	54	4
21 Apr 2017	17	21:30 - 22:04	29	317	49	10
25 Apr 2017	18	00:23 - 01:53	21	15	46	7
27 Apr 2017	19	22:54 - 23:17	15	33	49	8
28 Apr 2017	20	21:07 - 01:19	17	179	49	6
29 Apr 2017	21	03:22 - 03:56	27	147	67	7
09 May 2017	22	03:43 - 04:05	18	131	44	7
20 May 2017	23	18:43 - 19:06	21	321	15	17
21 May 2017	24	00:01 - 00:23	15	160	14	7
23 May 2017	25	03:23 - 03:45	26	155	45	10
30 Jun 2017	26	02:38 - 03:23	18	176	27	11
03 Jul 2017	27	00:23 - 01:08	24	167	30	12

Continued on next page

Table 4.1 – *Continued from previous page*

Date	Events	Time interval (UT)	wavelength (km)	Azimuth (°)	Velocity (m/s)	Period (min)
21 Aug 2017	28	00:00 - 00:34	26	145	64	7
	29	00:12 - 00:34	22	39	52	7
26 Aug 2017	30	00:00 - 00:34	86	268	52	29
31 Aug 2017	31	01:53 - 02:04	16	148	31	9
16 Sept 2017	32	18:41 - 19:03	11	154	44	6
18 Sept 2017	33	19:27 - 15:50	12	344	20	10
23 Sept 2017	34	18:10 - 18:33	13	14	23	7
28 Sept 2017	35	01:19 - 01:53	12	150	34	6
29 Sept 2017	36	02:15 - 02:49	65	31	57	18
01 Oct 2017	37	01:42 - 02:04	20	168	39	8
	38	01:53 - 02:16	19	188	12	27
02 Oct 2017	39	01:52 - 02:03	24	119	54	8
09 Oct 2017	40	20:04 - 20:49	15	303	22	12
12 Oct 2017	41	18:37 - 19:11	11	108	14	27
17 Oct 2017	42	20:56 - 21:30	20	150	15	24
20 Oct 2017	43	02:27 - 02:49	23	39	49	8
21 Oct 2017	44	18:56 - 19:18	19	273	12	8
22 Oct 2017	45	01:41 - 02:04	58	49	46	21
	46	01:41 - 02:37	16	149	21	13
22 Nov 2017	47	21:20 - 21:42	18	273	9	31
23 Nov 2017	48	21:43 - 22:40	11	52	13	17
07 Dec 2017	49	21:23 - 21:23	11			
10 Dec 2017	50	20:41 - 20:41	16			
13 Dec 2017	51	01:08 - 01:19	14	22	21	50
18 Dec 2017	52	20:35 - 20:46	13	322	17	5
20 Dec 2017	53	20:36 - 20:36	13			

A summary of the number of gravity wave events observed in each season are shown in Table 4.3. It can be seen from this table that the occurrence of AGW events was larger in summer and

spring, while winter had the least occurrence of AGWs mainly due to data being contaminated by clouds or lack of data recording for technical reasons during the winter days.

Table 4.2: Months assigned to each of the seasons.

Season	Months
Summer	December, January, February
Autumn	March, April, May
Winter	June, July, August
Spring	September, October, November

Table 4.3: Number of gravity wave events observed per season.

Season	Number of nights with waves	Total events
Summer	16	17
Autumn	13	13
Winter	5	6
Spring	15	17

4.1 Seasonal characteristics of gravity wave parameters

For consistency, the seasonal statistical analysis was performed for gravity waves where all their parameters could be estimated. This means that the results presented here are 49 out of 53 events. This section also shows histograms of the distribution of calculated gravity wave parameters. The propagation directions are defined using azimuth as follows:

- north: 337.5° - 22.5°
- northeast: 22.5° - 67.5°

– east: 67.5° - 112.5°

– southeast: 112.5° - 157.5°

– south: 157.5° - 202.5°

– southwest: 202.5° - 247.5°

– west: 247.5° - 292.5°

– northwest: 292.5° - 337.5°

Figure 4.1 shows the distribution of the wave parameters for the AGWs detected during the summer season. The horizontal wavelengths of AGWs during this season are less than 40 km and phase speed is distributed between 10 and 90 m/s, although the majority of the AGWs ($\sim$ 61%) have speeds between 30 and 50 m/s. Their periods are mostly less than 20 minutes with one event between 25 and 30 minutes and another event between 45 and 50 minutes. The waves favor a southeast propagation direction.

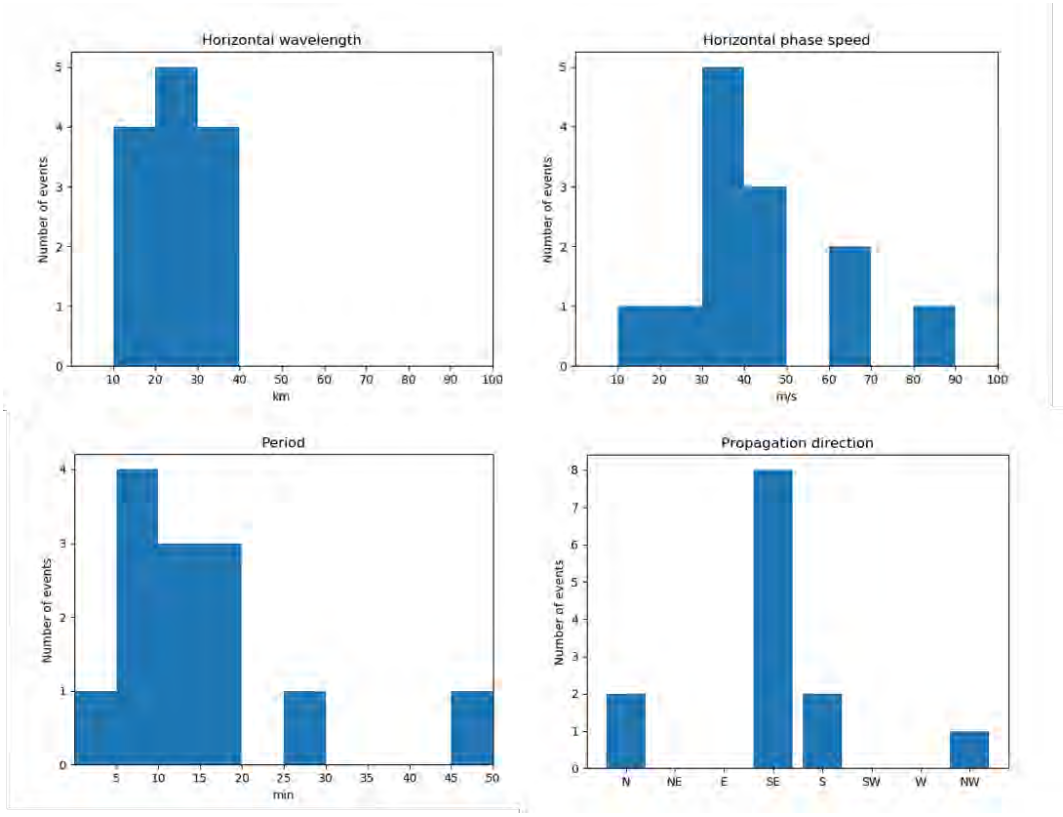

Figure 4.1: Distribution of gravity wave parameters in summer.

The AGW parameters calculated for the autumn months are seen in Figure 4.2 showing horizontal wavelengths that are below 30 km, and phase speeds distributed between 10 and 90 m/s, with a peak at 40 - 50 m/s. The AGWs during this season have periods less than 20 minutes, with a peak at 5 - 10 minutes. Their propagation is either north or south, but most of them ($\sim$ 61%) propagate in the southerly direction.

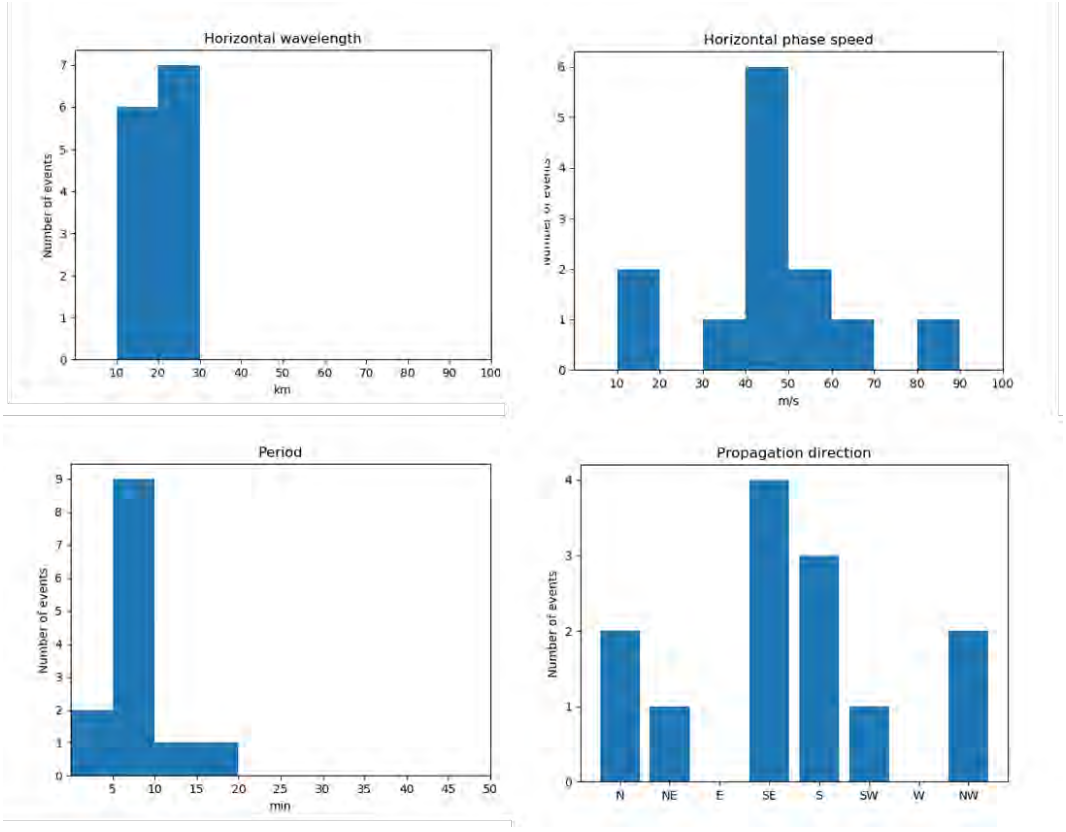

Figure 4.2: Distribution of gravity wave parameters in autumn.

Figure 4.3 presents the calculated wave parameters for gravity waves observed during the winter months. The horizontal wavelengths of AGWs during this season are mostly between 10 and 30 km, with only one event having a wavelength between 80 and 90 km. Half of the events have speeds that are between 20 and 40 m/s and the other half are between 50 and 70 m/s. They mostly have periods between 5 and 15 minutes, and only one gravity wave had a period between 25 and 30 minutes. The propagation of these waves is distributed between northeast, southeast, south and west propagation directions, however the majority ($\sim$ 67%) have a southward propagation.

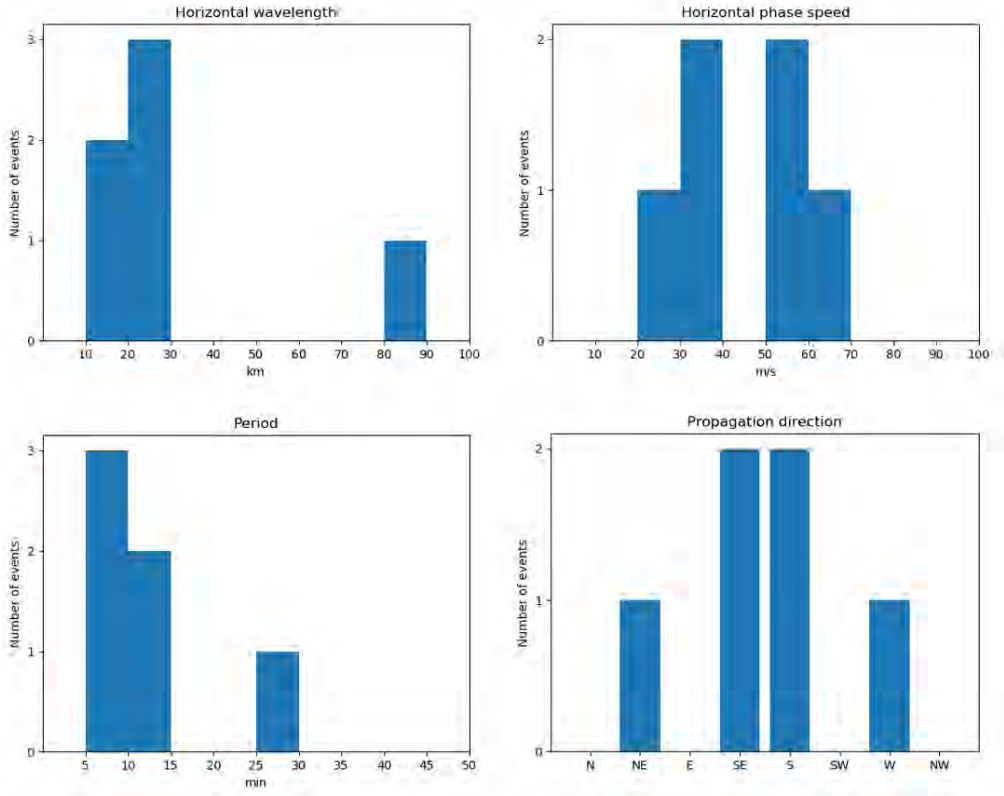

Figure 4.3: Distribution of gravity wave parameters in winter.

The calculated wave parameters for the AGWs observed during the spring months are given in Figure 4.4. This figure shows that most of the AGWs during this season have horizontal wavelengths between 10 and 30 km, with a peak at 10 - 20 km and only two events having wavelengths between 50 and 70 km. They also have phase speeds of less than 60 m/s, as well as periods between 5 and 35 minutes, with a peak at 5 - 10 minutes. They have no preferred propagation direction.

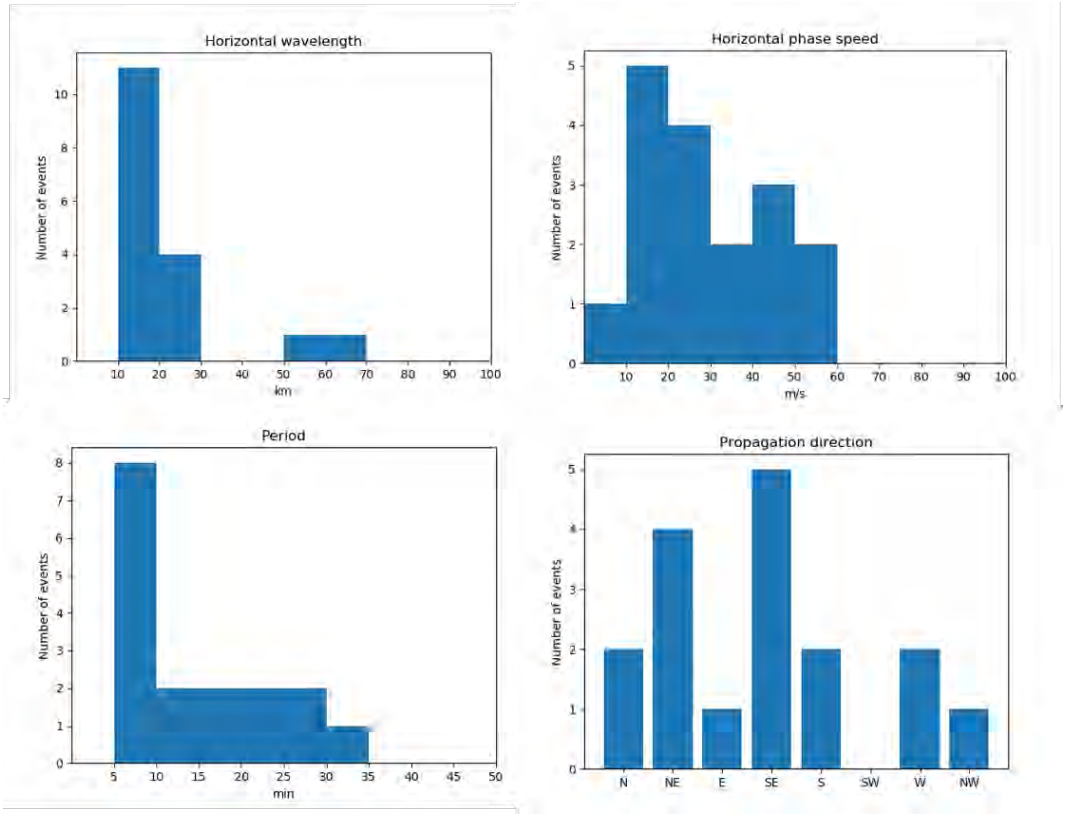

Figure 4.4: Distribution of gravity wave parameters in spring.

4.2 Discussion

The first goal of this project was to determine the wave parameters, such as period, wavelength, speed and propagation direction from the measurements of the 557.7 nm airglow emission. The results obtained showed that the AGWs had horizontal wavelengths almost evenly distributed between 10 and 40 km in summer, and mostly between 10 and 30 km in autumn, winter and spring. The AGWs in summer favoured a southeastward propagation, while they favoured a southward propagation in autumn and winter. There was no obvious trend in propagation direction for the AGWs observed in spring. During all seasons except winter, the majority of the AGWs had phase speeds < 50 m/s. The favoured phase speed of AGWs was 40 - 50 m/s in autumn, and 30 - 50 m/s in summer, but the AGWs in winter had a bimodal speed distribution of 20 - 40 and 50 - 70 m/s. In all seasons, the majority of the AGWs had periods < 20 minutes, but only those in autumn and spring had a dominant peak at 5 - 10 minutes.

The results discussed above are similar to those reported by Walterscheid et al. [1999] using *OH*

and O_2 emissions at Adelaide, Australia (30° S, 138° E) whereby they observed wavelengths that were a few tens of kilometres, and periods between 5 and 20 minutes. However, their phase speeds were slightly higher (ranging between 50 and 80 m/s) than the ones reported in this study. Another study that shows some similar results to ours was done by Suzuki et al. [2004] over Darwin, Australia (12.4° S, 131.0° E). They reported gravity waves with wavelengths that were $<$ 90 km, with a favoured range of 30 - 50 km, and phase speeds between 30 and 60 m/s. While the propagation results of their study agrees with ours in terms of the AGWs preferring southward propagation in summer and winter, they also found that the north was equally favoured in winter, which is not the case in this study. They also found AGWs that propagated in the zonal direction in spring, autumn and winter, while our study only found zonal propagation AGWs in spring. Teitelbaum & Petitdidier [1978] reported that after sunset (16:00 UT) most gravity waves observed short-period oscillations that had a period between 2 and 15 minutes and Kirchhoff et al. [1986] reported a similar observation from a study done in Brazil. The results show similar wave periods as those observed in this study where a majority of the waves with periods between 5 and 15 minutes occurred after sunset (16:00 UT).

Nakamura et al. [1999] found waves with horizontal wavelengths that range from 5 to 60 km, phase speeds distribution of $0 - 100$ m/s, and periods between 5 and 30 minutes over Shigaraki, Japan (35° N, 136° E). The wavelengths are within the same range observed in this study however the phase speeds reach higher values over 70 m/s. With regards to the seasonal variation of the AGW wavelengths, they found that spring and autumn had horizontal wavelengths of $15 - 35$ km and not many of the waves observed are less than 15 km. This range is not so different from that obtained from our study which showed AGW wavelengths between 10 and 30 km in spring and autumn of which many were between 10 and 20 km. They also reported that summer and winter AGWs had wavelengths spread between 5 and 35 km, which is also not different to this study where wavelengths were below 40 km in these seasons. They reported periods between 5 and 10 minutes as the most common in all the seasons which is similar to what was observed for AGWs in autumn and spring in this study. They found a peak of AGW phase speed at around 20 - 30 m/s in summer and winter, which agrees with the speeds of our winter AGWs, but is smaller than our summer AGWs. The majority of the AGWs in spring had speeds of 40 - 75 m/s in their study, where in ours the speeds were less than 60 m/s.

Taylor et al. [2009] analysed small-scale gravity waves ($\lambda_x < 100$ km), period ($\tau < 30$ minutes)

at two low latitude sites in Brazil, Cariri (7.4 °S, 36.5 °W) and Brasilia (14.8 °S, 47.6 °W). They observed AGWs with horizontal wavelengths in the range of 10 - 25 km for Cariri and 15 - 30 km for Brasilia, which is similar to our results in that wavelengths are below 30 km for most seasons except summer. Also similar to our results they found that both sites showed a preference for phase speeds of 30 - 60 m/s but had a range of 20 - 80 m/s. The periods for both sites were relatively short and clustered around 8 - 11 minutes and typically ranged between 5 - 20 minutes, also in agreement with periods reported in our study. The favoured propagation direction of southeast observed in this study for summer AGWs is different in comparison with Cariri but similar with Brasilia where AGWs favoured northeast and east - southeast propagation directions respectively.

Essien et al. [2018] also studied small scale (i.e wavelengths less than 50 km) and medium scale (wavelengths greater than 50 km) mesospheric gravity waves over Cariri (7.4° S, 36.5° W) but over a longer time period of September 2000 - December 2010. Since the majority of the AGWs observed in our study have wavelengths corresponding to the small scale AGWs as per Essien et al. [2018], we will compare our results to the characteristics of their small scale waves. They reported that their AGWs had horizontal wavelengths that ranged from 5 to 50 km with the majority of the events distributed between 10 and 35 km. Their period were in the range of 5 - 50 minutes with the peak at 5 to 10 minutes, while their phase speeds had a peak at 10 to 70 m/s with 20 to 40 m/s being the most common. The results reported by Taylor et al. [2009] for the same station were slightly different, probably due to the fact that they used a smaller set of data. Most of the characteristics determined for the AGWs observed in this study agree with those reported by Essien et al. [2018]. For example, periods of AGWs were less than 50 minutes, with a peak of 5 - 10 minutes in autumn and spring. In addition, their wavelengths were also mostly less than 50 km. However we note a difference in the propagation direction of AGWs of those reported in this study versus those reported by Essien et al. [2018]. They found that generally the AGWs preferred a northeastward propagation, but in summer and autumn a southeastward was preferred in addition to northeastward and in spring a northwest and southeast propagation direction was preferred. However in this study, only the southeastward propagation was favoured and in autumn as well as winter the AGWs preferred a more south propagation direction.

Suzuki et al. [2004] reported that the seasonal variation of gravity wave occurrence rate were

high in the spring (even though it contains only 1 month of data), and low in summer. Wu & Killeen [1996] reported for Peach Mountain Observatory, Michigan (42.3° N, 83.7° W) that the mesospheric gravity waves activity depends highly on the season, peaking in summer and have a low activity in winter. Therefore the results in our study mostly agree with these studies as we observed more AGWs in summer and spring and least AGWs in winter.

Only 9 out of 49 (i.e. $\sim 18\%$) AGWs with calculated phase speeds had velocities below 20 m/s. The low detection of AGWs with these low speeds could be due to wind filtering as Taylor et al. [1997] and Essien et al. [2018] reported that AGWs with speeds below 20 m/s are susceptible to background wind filtering in the stratosphere and lower mesosphere. Also, Taylor et al. [1997] and Nakamura et al. [1999] reported that these AGWs might be instability features generated in situ, i.e. ripples. D. Fritts et al. [2008] noted that wind filtering of AGWs and the location of the wave source were the two main factors that could create the observed anisotropy of AGW propagation.

Another potential source of gravity waves is the solar terminator (ST) which is the region of boundary separating the daytime and nighttime on earth [Beer, 1973; Raitt & Clark, 1973; Song et al., 2013]. It is characterized by sudden changes in the temperature and pressure of the atmosphere. The prediction was proven theoretically by Somsikov & Trotskii [1975] that through its supersonic and subsonic motion it can cause AGWs. Somsikov [1991] went on to say that the abrupt changes resulted in pressure instabilities which as a result of gravity reacting to these disturbances will cause AGWs which travel in the same direction (East to West) as the solar terminator. In this study, however, the solar terminator is not the source of the gravity waves since only one AGW occurs within a couple of hours after the passage of the solar terminator and propagate westward (i.e. event on 21 Oct 2017), but the majority of the AGWs are observed several hours post solar terminator and don't propagate in the expected direction.

Chapter 5

Conclusions and Future works

This thesis presented a statistical analysis of AGWs from the 557.7 nm airglow emission at ∼97 km altitude. The data was obtained using an airglow imager located in Sutherland, South Africa. The wavelengths were determined using the propagation vector method, velocity was determined using the cross correlation of 1D FFT and the period was determined using the equation that relates wavelength and velocity. The results were then used to perform statistical analysis for 2017.

5.1 Conclusions

This project determined the properties of night-time gravity waves (AGWs) over South Africa using a multi-wavelength airglow all-sky imager (ASI) in Sutherland, South Africa. The objectives were to 1) determine the wave parameters such as wavelength, speed, period and propagation azimuth, from measurements of the 557.7 nm airglow emissions, and 2) determine statistical characteristics of these parameters. The conclusions from this study are as follows:

The study visually identified 53 AGWs from 206 nights with clear visibility conditions. These AGWs had wavelengths less than 90 km, speeds less than 90 m/s, periods less than 50 minutes and propagation of AGWs didn't have a clear preference in spring, but favoured a southeast direction in summer, and southward in autumn and winter. The AGWs observed were 17 in summer and spring, 13 in autumn and 6 in winter season, however, for seasonal statistical analysis only those AGWs where all the gravity wave parameters could be estimated were used. The majority of AGWs in our study had wavelengths between 10 and 40 km in summer and 10

- 30 km in autumn, winter and spring. Their favoured speeds were between 40 and 50 m/s in autumn, and in the range of 30 - 50 m/s in summer, but the AGWs in winter had a bimodal speed distribution of 20 - 40 and 50 - 70 m/s. The majority of the observed AGWs had periods that were less than 20 minutes in all seasons. In addition, with a dominant peak around 5 - 10 minutes in autumn and spring. There was no favoured propagation direction for spring, but AGWs favoured a southeastward propagation in summer, and a southward propagation in autumn and winter.

5.2 Future Works

A proper investigation of possible sources that could be responsible for the AGWs activity observed was not possible due to time constraint, and the work can be expanded by using satellite and radar measurements to determine possible sources of the observed AGWs. Other investigations that can be done with this data are to:

- determine the wave parameters such as wavelength, phase speed, period and propagation azimuth from measurements of the 630.0 nm and the 589.0 nm airglow emissions.
- determine if the thunderstorm generated gravity waves can modulate mesospheric disturbances (e.g. sprites).
- find out whether there is a dominating source for gravity waves of different scales.

References

Afraimovich, E. L., Perevalova, N. P., Plotnikov, A., & Uralov, A. (2001). The shock-acoustic waves generated by earthquakes. *Annales Geophysicae*, *19*(4), 395–409. doi: https://doi.org/10.5194/angeo-19-395-2001

Amorim, D. C. M., Pimenta, A. A., Bittencourt, J. A., & Fagundes, P. R. (2011). Long-term study of medium-scale traveling ionospheric disturbances using OI 630 nm all-sky imaging and ionosonde over Brazilian low latitudes. *Journal of Geophysical Research: Space Physics*, *116*(A6), A06312. doi: https://doi.org/10.1029/2010JA016090.

Andrews, D. G., Leovy, C. B., & Holton, J. R. (1987). *Middle atmosphere dynamics* (1st ed.). Academic press. (ISBN:978-0120585762)

Arikan, F., & Yarici, A. (2017). Spectral investigation of traveling ionospheric disturbances: IONOLAB-FFT. *Geodesy and Geodynamics*, *8*(5), 297–304. doi: https://doi.org/10.1016/j.geog.2017.05.002

Bakken, I. (2015). *A comparison of gravity wave parameters derived from the analysis of a three-field photometer with imagers* (Unpublished master's thesis). Norwegian University of Science and technology, Norway.

Beer, T. (1973). Supersonic generation of atmospheric waves. *Nature*, *242*(5392), 34–34. doi: https://doi.org/10.1038/242034a0

Beer, T. (1974). *Atmospheric waves.* Wiley, New York. (ISBN:978-0470061855)

Beer, T. (1978). On atmospheric wave generation by the terminator. *Planetary and Space Science*, *26*(2), 185–188. doi: https://doi.org/10.1002/qj.49709540402

Brasseur, G. P., & Solomon, S. (2006). *Aeronomy of the middle atmosphere: Chemistry and physics of the stratosphere and mesosphere* (Vol. 32). Springer Science & Business Media. (ISBN: 978-1402032844) doi: https://doi.org/10.1007/1-4020-3824-0

Bretherton, F. P. (1969). Momentum transport by gravity waves. *Quarterly Journal of the Royal Meteorological Society*, *95*(404), 213–243. doi: https://doi.org/10.1002/qj.49709540402

Chamberlain, J. W. (2016). *Physics of the Aurora and Airglow: International Geophysics Series, Vol. 2* (1st ed., Vol. 2). Elsevier. (ISBN:978-1483222530)

Chapagain, N. P. (2011). Dynamics of equatorial spread F using ground-based optical and radar measurements, Ph.D. Thesis, Utah State University, Logan, Utah.

Chapman, S. (1950). Upper atmospheric nomenclature. *Journal of Geophysical Research*, *55*(4), 121–124. doi: https://doi.org/10.1029/JZ055i004p00395

Chattopadhyay, R., & Midya, S. (2006). Airglow emissions: fundamentals of theory and experiment. *Indian Journal of Physics and proceedings of the Indian Association for the cultivation of science - New Series*, *80*(2), 115.

Chimonas, G. (1970). The equatorial electrojet as a source of long period travelling ionospheric disturbances. *Planetary and Space Science*, *18*(4), 583–589. doi: https://doi.org/10.1029/GM018p0698

Costantino, L., Heinrich, P., Mzé, N., & Hauchecorne, A. (2015). Convective gravity wave propagation and breaking in the stratosphere: comparison between WRF model simulations and lidar data. *Annales Geophysicae*, *33*(9), 1155-1171. doi: https://doi.org/10.5194/angeo-33-1155-2015

Davies, K. (1990). *Ionospheric radio* (1st ed.) (No. 31). IET. (ISBN:978-0863411861)

Dolas, P. M., & Kishore Kumar, K. (2009). Retrieval of static stability parameter from the radiosonde/rawinsonde ascent rate profiles: a wavelet approach. *Annales Geophysicae*, *27*(2), 547–553. doi: https://doi.org/10.5194/angeo-27-547-2009

Elvey, C. T. (1950). Note on the Spectrum of the Airglow in the Red Region. *The Astrophysics Journal*, *111*, 432 - 433. doi: https://doi.org/10.1086/145278

Essien, P., Paulino, I., Wrasse, C. M., Campos, J. A. V., Paulino, A. R., Medeiros, A. F., ... Lins, A. N. (2018). Seasonal characteristics of small-and medium-scale gravity waves in the mesosphere and lower thermosphere over the Brazilian equatorial region. *Annales Geophysicae*, *36*(3), 899–914. doi: https://doi.org/10.5194/angeo-36-899-2018

Francis, S. H. (1974). A theory of medium-scale traveling ionospheric disturbances. *Journal of Geophysical Research*, *79*(34), 5245–5260. doi: https://doi.org/10.1029/JA079i034p05245

Fritts, D., Vadas, S., Riggin, D., Abdu, M., Batista, I., Takahashi, H., ... Fejer, B. G. (2008). Gravity wave and tidal influences on equatorial spread F based on observations during the spread F experiment SpreadFEx. *Annales Geophysicae*, *26*(11), 3235–3252. doi: https://doi.org/10.5194/angeo-26-3235-2008

Fritts, D. C. (1995). Gravity wave forcing and effects in the mesosphere and lower thermosphere. *The Upper Mesosphere and Lower Thermosphere: A Review of Experiment and Theory*, *87*, 89–100. doi: http://doi.org/10.1029/GM087p0121

Fritts, D. C., & Alexander, M. J. (2003). Gravity wave dynamics and effects in the middle atmosphere. *Reviews of Geophysics*, *41*(1), 1003. doi: https://doi.org/10.1029/2001RG000106

Garcia, F., Taylor, M. J., & Kelley, M. (1997). Two-dimensional spectral analysis of mesospheric airglow image data. *Applied Optics*, *36*(29), 7374–7385. doi: https://doi.org/10.1364/AO.36.007374

Garcia, F. J. (1999). *Atmospheric studies using all-sky imaging of airglow layers* (1st ed.). Cornell University, Jan.

Habarulema, J. B., Katamzi, Z. T., & McKinnell, L.-A. (2013). Estimating the propagation characteristics of large-scale traveling ionospheric disturbances using ground-based and satellite data. *Journal of Geophysical Research: Space Physics*, *118*(12), 7768–7782. doi: https://doi.org/10.1002/2013JA018997

Habarulema, J. B., Katamzi, Z. T., & Yizengaw, E. (2015). First observations of poleward large-scale traveling ionospheric disturbances over the African sector during geomagnetic storm conditions. *Journal of Geophysical Research: Space Physics*, *120*(8), 6914–6929. doi: https://doi.org/10.1002/2015JA021066

Habarulema, J. B., Katamzi, Z. T., Yizengaw, E., Yamazaki, Y., & Seemala, G. (2016). Simultaneous storm time equatorward and poleward large-scale TIDs on a global scale. *Geophysical Research Letters*, *43*(13), 6678–6686. doi: https://doi.org/10.1002/2016GL069740

Habarulema, J. B., Yizengaw, E., Katamzi-Joseph, Z. T., Moldwin, M. B., & Buchert, S. (2018). Storm time global observations of large-scale tids from ground-based and in situ satellite measurements. *Journal of Geophysical Research: Space Physics*, *123*(1), 711–724. doi: https://doi.org/10.1002/2017JA024510

Hajkowicz, L. (1990). A global study of large scale travelling ionospheric disturbances (TIDs) following a step-like onset of auroral substorms in both hemispheres. *Planetary and Space Science*, *38*(7), 913–923. doi: https://doi.org/10.1016/0032-0633(90)90058-X

Hatlen, M. (2013). *On-board, Fourier-based image-analysis system for satellite observation of gravity waves* (Unpublished master's thesis). Institute for Physics, Norwegian University of Science and Technology.

Hecht, J. (2004). Instability layers and airglow imaging. *Reviews of Geophysics*, *42*(1), RG1001. doi: https://doi.org/10.1029/2003RG000131

Hernandez, G., & Roble, R. (1978). Observations of large-scale thermospheric waves during geomagnetic storms. *Journal of Geophysical Research: Space Physics*, *83*(A12), 5531–5538. doi: https://doi.org/10.1029/JA083iA12p05531

Hickey, D. A., Martinis, C. R., Mendillo, M., Baumgardner, J., Wroten, J., & Milla, M. (2018). Simultaneous 6300 Å airglow and radar observations of ionospheric irregularities and dynamics at the geomagnetic equator. *Annales Geophysicae*, *36*(2), 473–487. doi: https://doi.org/10.5194/angeo-36-473-2018

Hines, C. O. (1960). Internal atmospheric gravity waves at ionospheric heights. *Canadian Journal of Physics*, *38*(11), 1441–1481. doi: https://doi.org/10.1139/p60-150

Hines, C. O. (1964). Atmospheric gravity waves - A new toy for the wave theorist. *Radio Science*, *69D*, 375-380. doi: https://doi.org/10.1029/GM018p0198

Hines, C. O., & Hines, C. O. (1974). *The Upper Atmosphere in Motion. In The Upper Atmosphere in Motion, C.O. Hines (Ed).* doi: https://doi.org/10.1029/GM018p0014

Hocke, K., Schlegel, K., et al. (1996). A review of atmospheric gravity waves and travelling ionospheric disturbances: 1982–1995. *Annales Geophysicae*, *14*(9), 917 - 940. doi: https://doi.org/10.1007/s00585-996-0917-6

Kamide, Y., & Chian, A. C.-L. (2007). *Handbook of the solar-terrestrial environment.* Berlin: Springer. (ISBN:978-3-540-46314-6)

Katamzi, Z. T., & Habarulema, J. B. (2014). Traveling ionospheric disturbances observed at South African midlatitudes during the 29–31 October 2003 geomagnetically disturbed period. *Advances in Space Research*, *53*(1), 48–62. doi: https://doi.org/10.1016/j.asr.2013.10.019

Kelley, M. C. (2009). *The Earth's Ionosphere: Plasma Physics and Electrodynamics* (2nd ed.). Academic press. (ISBN: 9780120884254)

Kirchhoff, V., Batista, P., Clemesha, B., & Simonich, D. (1986). The twilight sodium layer. *Journal of Geophysical Research: Atmospheres*, *91*(D12), 13303–13307. doi: https://doi.org/10.1029/JD091iD12p13303

Klausner, V., Fagundes, P., Sahai, Y., Wrasse, C., Pillat, V., & Becker-Guedes, F. (2009). Observations of GW/TID oscillations in the F2 layer at low latitude during high and low solar activity, geomagnetic quiet and disturbed periods. *Journal of Geophysical Research: Space Physics*, *114*(A2). doi: https://doi.org/10.1029/2008JA013448

Kohl, H., Rüster, R., & Schlegel, K. (1996). *Modern Ionospheric Science. A Collection of Articles Published on the Occasion of the Anniversary:"50 Years of Ionospheric Research in Lindau".* European Geophysical Society, Katlenburg-Lindau. (ISBN:978-3980486217)

Krankowski, A., Zakharenkova, I., Krypiak-Gregorczyk, A., Shagimuratov, I. I., & Wielgosz, P. (2011). Ionospheric electron density observed by FORMOSAT-3/COSMIC over the European region and validated by ionosonde data. *Journal of Geodesy*, *85*(12), 949–964. doi: https://doi.org/10.1007/s00190-011-0481-z

Leckner, B. (1978). The spectral distribution of solar radiation at the earth's surface—elements of a model. *Solar Energy*, *20*(2), 143–150. doi: https://doi.org/10.1016/0038-092X(78)90187-1

Makela, J. J., & Kelley, M. (2003). Field-aligned 777.4-nm composite airglow images of equatorial plasma depletions. *Geophysical Research Letters*, *30*(8). doi: https://doi.org/10.1029/2003GL017106

Makela, J. J., Kelley, M. C., González, S. A., Aponte, N., & McCoy, R. P. (2001). Ionospheric topography maps using multiple-wavelength all-sky images. *Journal of Geophysical Research: Space Physics*, *106*(A12), 29161–29174. doi: https://doi.org/10.1029/2000JA000449

Makela, J. J., Miller, E., & Talaat, E. (2010). Nighttime medium-scale traveling ionospheric disturbances at low geomagnetic latitudes. *Geophysical Research Letters*, *37*(24). doi: https://doi.org/10.1029/2010GL045922

Martinis, C., Baumgardner, J., Mendillo, M., Wroten, J., MacDonald, T., Kosch, M., ... Umbriaco, G. (2019). First conjugate observations of medium-scale traveling ionospheric disturbances (MSTIDs) in the Europe-Africa longitude sector. *Journal of Geophysical Research: Space Physics*, *124*(3), 2213–2222. doi: https://doi.org/10.1029/2018JA026018

Martinis, C., Baumgardner, J., Wroten, J., & Mendillo, M. (2018). All-sky-imaging capabilities for ionospheric space weather research using geomagnetic conjugate point observing sites. *Advances in Space Research*, *61*(7), 1636–1651. doi: https://doi.org/10.1016/j.asr.2017.07.021

Martinis, C., & Mendillo, M. (2007). Equatorial spread F-related airglow depletions at Arecibo and conjugate observations. *Journal of Geophysical Research: Space Physics*, *112*, A10310. doi: https://doi.org/10.1029/2007JA012403

Martinis, C., Wilson, J., Zablowski, P., Baumgardner, J., Aballay, J. L., Garcia, B., ... Otero, L. (2013). A new method to estimate cloud cover fraction over El Leoncito Observatory from an all-sky imager designed for upper atmosphere studies. *Publications of the Astronomical Society of the Pacific*, *125*(923), 56–67. doi: http://iopscience.iop.org/article/10.1086/669255

Matamba, T. M., Habarulema, J. B., & McKinnell, L.-A. (2015). Statistical analysis of the ionospheric response during geomagnetic storm conditions over South Africa using ionosonde and GPS data. *Space Weather*, *13*(9), 536–547. doi: https://doi.org/10.1002/2015SW001218

Mayr, H., Harris, I., Herrero, F., & Pesnell, W. (1991). Transfer Function Model (TFM) and Gravity Waves. *Journal of Geomagnetism and Geoelectricity*, *43*(Supplement1), 525–536. doi: https://doi.org/10.5636/jgg.43.Supplement1_525

McEwan, M. J., & Phillips, L. F. (1975). *Chemistry of the atmosphere* (1st ed.). Edward Arnold, London. (ISBN:978-0713124774)

Mendillo, M., Baumgardner, J., Nottingham, D., Aarons, J., Reinisch, B., Scali, J., & Kelley, M. (1997). Investigations of thermospheric-ionospheric dynamics with 6300-Å images from the arecibo observatory. *Journal of Geophysical Research: Space Physics*, *102*(A4), 7331–7343. doi: https://doi.org/10.1029/96JA02786

Mondal, S., Srivastava, A., Yadav, V., Sarkhel, S., Krishna, M. S., Rao, Y. K., & Singh, V. (2019). All sky airglow imaging observations from Hanle, Leh Ladakh, India: Image analyses and first results. *Advances in Space Research*, *64*(10), 1926–1939. doi: https://doi.org/10.1016/j.asr.2019.05.047

Moon, J., Lee, W., Song, C., Lee, S., Heo, S., Shvidenko, A., ... others (2017). An introduction to mid-latitude ecotone: Sustainability and environmental challenges. *Siberian Journal of Forest Science*, *6*, 41–51. doi: https://doi.org/10.15372/SJFS20170603

Mukhtarov, P., Pancheva, D., Andonov, B., & Pashova, L. (2013). Global TEC maps based on GNSS data: 1. Empirical background TEC model. *Journal of Geophysical Research: Space Physics*, *118*(7), 4594–4608. doi: https://doi.org/10.1002/jgra.50413

Naero, K. (2013). *Gravity Wave Refraction in the Atmosphere: Ray tracing versus Geometric Location from a Single Image* (Unpublished master's thesis). Norwegian Univeristy of Science and Technology.

Nakamura, T., Higashikawa, A., Tsuda, T., & Matsushita, Y. (1999). Seasonal variations of gravity wave structures in OH airglow with a CCD imager at Shigaraki. *Earth, Planets and Space*, *51*(7-8), 897–906. doi: https://doi.org/10.1186/BF03353248

Nappo, C. J. (2013). *An introduction to atmospheric gravity waves* (1st ed.). International Geophysics Series; Elsevier Science: San Diego, CA, USA. (ISBN:978-0123852236)

Nielsen, K., Taylor, M. J., Stockwell, R., & Jarvis, M. (2006). An unusual mesospheric bore event observed at high latitudes over Antarctica. *Geophysical Research Letters*, *33*(7). doi: https://doi.org/10.1029/2005GL025649

Otsuka, Y., Shiokawa, K., Ogawa, T., & Wilkinson, P. (2004). Geomagnetic conjugate observations of medium-scale traveling ionospheric disturbances at midlatitude using all-sky airglow imagers. *Geophysical Research Letters*, *31*, L15803. doi: https://doi.org/10.1029/2004GL020262

Parkinson, M. L., Polglase, R., Fejer, B. G., Scherliess, L., Dyson, P., & Ujmaia, S. (2001). Seasonal and magnetic activity variations of ionospheric electric fields above the southern mid-latitude station, Bundoora, Australia. *Annales Geophysicae*, *19*(5), 521 –532. doi: https://doi.org/10.5194/angeo-19-521-2001

Raitt, W., & Clark, D. (1973). Wave-like disturbances in the ionosphere. *Nature*, *243*(5409), 508–509. doi: https://doi.org/10.1038/243508a0

Rishbeth, H. (1968). Solar eclipses and ionospheric theory. *Space Science Reviews*, *8*(4), 543–554. doi: https://doi.org/10.1007/BF00175006

Roble, R. G. (1995). Energetics of the mesosphere and thermosphere. *The Upper Mesosphere and Lower Thermosphere: A Review of Experiment and Theory, Geophys. Monogr. Ser*, *87*, 1–21. doi: http://doi.org/10.1029/GM087p0001

Salby, M. L. (1996). *Fundamentals of atmospheric physics* (1st ed.). Elsevier. (ISBN:978-0-12-615160-2)

Shiokawa, K., Otsuka, Y., Ihara, C., Ogawa, T., & Rich, F. (2003). Ground and satellite observations of nighttime medium-scale traveling ionospheric disturbance at midlatitude. *Journal of Geophysical Research: Space Physics*, *108*(A4), 1145. doi: https://doi.org/10.1029/2002JA009639

Smith, A. K. (2004). Physics and chemistry of the mesopause region. *Journal of Atmospheric and Solar-Terrestrial Physics*, *66*(10), 839–857. doi: https://doi.org/10.1016/j.jastp.2004.01.032

Smith, S., Friedman, J., Raizada, S., Tepley, C., Baumgardner, J., & Mendillo, M. (2005). Evidence of mesospheric bore formation from a breaking gravity wave event: Simultaneous imaging and lidar measurements. *Journal of atmospheric and solar-terrestrial physics*, *67*(4), 345–356. doi: https://doi.org/10.1016/j.jastp.2004.11.008

Solomon, S., Portmann, R., Sanders, R., & Daniel, J. (1998). Absorption of solar radiation by water vapor, oxygen, and related collision pairs in the Earth's atmosphere. *Journal of Geophysical Research: Atmospheres*, *103*(D4), 3847–3858. doi: https://doi.org/10.1029/97JD03285

Somsikov, V. (1991). Waves in the atmosphere due to the solar terminator. *Geomagnetizm and Aeronomiya.*, *31*, 1–12.

Somsikov, V., & Ganguly, B. (1995). On the formation of atmospheric inhomogeneities in the solar terminator region. *Journal of Atmospheric and Terrestrial Physics*, *57*(12), 1513–1523. doi: https://doi.org/10.1016/0021-9169(95)00014-S

Somsikov, V., & Trotskii, B. (1975). Generation of disturbances in the atmosphere during the passage of the solar terminator through it. *International Journal of Geomagnetism and Aeronomy (USSR)(Engl. Transl.);(United States)*, *15*(5), 856-860.

Song, Q., Ding, F., Wan, W., Ning, B., Liu, L., Zhao, B., ... Zhang, R. (2013). Statistical study of large-scale traveling ionospheric disturbances generated by the solar terminator over China. *Journal of Geophysical Research: Space Physics*, *118*(7), 4583–4593. doi: https://doi.org/10.1002/jgra.50423

Ssessanga, N., Kim, Y. H., & Kim, E. (2015). Vertical structure of medium-scale traveling ionospheric disturbances. *Geophysical Research Letters*, *42*(21), 9156–9165. doi: https://doi.org/10.1002/2015GL066093

Suzuki, S., Shiokawa, K., Otsuka, Y., Ogawa, T., & Wilkinson, P. (2004). Statistical characteristics of gravity waves observed by an all-sky imager at Darwin, Australia. *Journal of Geophysical Research: Atmospheres*, *109*, D20S07. doi: https://doi.org/10.1029/2003JD004336

Takahashi, H., Clemesha, B., Sahai, Y., Batista, P., & Simonich, D. (1992). Seasonal variations of mesospheric hydrogen and ozone concentrations derived from ground-based airglow and

lidar observations. *Journal of Geophysical Research: Atmospheres*, *97*(D5), 5987–5993. doi: https://doi.org/10.1029/91JD03015

Takahashi, H., Taylor, M. J., Pautet, P.-D., Medeiros, A., Gobbi, D., Wrasse, C., ... others (2009). Simultaneous observation of ionospheric plasma bubbles and mesospheric gravity waves during the SpreadFEx Campaign. In (Vol. 27, pp. 1477–1487). doi: https://doi.org/10.5194/angeo-27-1477-2009

Takahashi, H., Wrasse, C. M., Figueiredo, C. A. O. B., Barros, D., Abdu, M. A., Otsuka, Y., & Shiokawa, K. (2018). Equatorial plasma bubble seeding by MSTIDs in the ionosphere. *Progress in Earth and Planetary Science*, *5*(1), 1–13. doi: https://doi.org/10.1186/s40645-018-0189-2

Taori, A., Parihar, N., Ghodpage, R., Dashora, N., Sripathi, S., Kherani, E., & Patil, P. (2015). Probing the possible trigger mechanisms of an equatorial plasma bubble event based on multistation optical data. *Journal of Geophysical Research: Space Physics*, *120*(10), 8835–8847. doi: https://doi.org/10.1002/2015JA021541

Taylor, M. J., & Hapgood, M. (1990). On the origin of ripple-type wave structure in the OH nightglow emission. *Planetary and space science*, *38*(11), 1421–1430. doi: https://doi.org/10.1016/0032-0633(90)90117-9

Taylor, M. J., Pautet, P.-D., Medeiros, A., Buriti, R., Fechine, J., Fritts, D., ... Sao Sabbas, F. (2009). Characteristics of mesospheric gravity waves near the magnetic equator, Brazil, during the SpreadFEx campaign. *Annales Geophysicae*, *27*(2), 461–472. doi: https://doi.org/10.5194/angeo-27-461-2009

Taylor, M. J., Pendleton Jr, W., Clark, S., Takahashi, H., Gobbi, D., & Goldberg, R. (1997). Image measurements of short-period gravity waves at equatorial latitudes. *Journal of Geophysical Research: Atmospheres*, *102*(D22), 26283–26299. doi: https://doi.org/10.1029/96JD03515

Taylor, M. J., Turnbull, D., & Lowe, R. (1995). Spectrometric and imaging measurements of a spectacular gravity wave event observed during the ALOHA-93 campaign. *Geophysical Research Letters*, *22*(20), 2849–2852. doi: https://doi.org/10.1029/95GL02948

Teitelbaum, H., & Petitdidier, M. (1978). Night-time variation of short period fluctuations (2–15 min) in the oxygen green line. *Journal of Atmospheric and Terrestrial Physics*, *40*(2), 223–227. doi: https://doi.org/10.1016/0021-9169(78)90027-2

Thome, G. (1968). Long-period waves generated in the polar ionosphere during the onset of magnetic storms. *Journal of Geophysical Research*, *73*(19), 6319–6336. doi: https://doi.org/10.1029/JA073i019p06319

Tricoli, U. (2015). Electromagnetic scattering with the GDT-matrix method: An application to irregular ice particles in cirrus, Ph.D. Thesis, Aix-Marseille University, France.

Vincent, R. A. (2015). The dynamics of the mesosphere and lower thermosphere: a brief review. *Progress in Earth and Planetary Science*, *2*(1), 1–13. doi: https://doi.org/10.1186/s40645-015-0035-8

Walterscheid, R., Hecht, J., Vincent, R., Reid, I., Woithe, J., & Hickey, M. (1999). Analysis and interpretation of airglow and radar observations of quasi-monochromatic gravity waves in the upper mesosphere and lower thermosphere over Adelaide, Australia (35 S, 138 E). *Journal of Atmospheric and Solar-Terrestrial Physics*, *61*(6), 461–478. doi: https://doi.org/10.1016/S1364-6826(99)00002-4

Walterscheid, R., Schubert, G., & Brinkman, D. (2001). Small-scale gravity waves in the upper mesosphere and lower thermosphere generated by deep tropical convection. *Journal of Geophysical Research: Atmospheres*, *106*(D23), 31825–31832. doi: https://doi.org/10.1029/2000JD000131

Webb, W. L. (1966). *Structure of the stratosphere and mesosphere* (Vol. 9). Academic Press New York. (ISBN:978-1483253091)

Winters, K. B., & Riley, J. J. (1992). Instability of internal waves near a critical level. *Dynamics of Atmospheres and Oceans*, *16*(3-4), 249–278. doi: https://doi.org/10.1016/0377-0265(92)90009-I

Wu, Q., & Killeen, T. (1996). Seasonal dependence of mesospheric gravity waves ($<$ 100 km) at Peach Mountain Observatory, Michigan. *Geophysical Research Letters*, *23*(17), 2211–2214. doi: https://doi.org/10.1029/96GL02168

Yntema, L. (1909). *On the brightness of the sky and the total amount of starlight* (1st ed., Vol. 22). Publications of the Kapteyn Astronomical Groningen. (ISBN:978-1313820295)